Linking Danube River activity to Alpine Ice-Sheet fluctuations during the last glacial (ca. 33–17 ka BP): Insights into the continental signature of Heinrich Stadials

Ruth Martinez-Lamas, Samuel S. Toucanne, Maxime Debret, Vincent Riboulot, Julien Deloffre, Audrey Boissier, Sandrine Chéron, Mathilde Pitel, Germain Bayon, Liviu Giosan, et al.

Linking Danube River Activity to Alpine Ice-Sheet Fluctuations during the Last Glacial (*ca.* 33-17 ka BP): insights into the continental signature of Heinrich Stadials

Ruth Martinez-Lamas[a,b,*], Samuel Toucanne[b], Maxime Debret[a], Vincent Riboulot[b], Julien Deloffre[a], Audrey Boissier[b], Sandrine Cheron[b], Mathilde Pitel[b], Germain Bayon[b], Liviu Giosan[c] & Guillaume Soulet[b]

[a] Normandie Univ., UNIROUEN, UNICAEN, CNRS, M2C, F-76000, Rouen, France
[b] IFREMER, Unité de Recherche Géosciences Marines, F-29280, Plouzané, France
[c] Department of Geology and Geophysics, Woods Hole Oceanographic Institution, 266 Woods Hole Road, Woods Hole, MA 02543, USA

* Corresponding author. E-mail address: *ruth.martinez-lamas1@univ-rouen.fr* (R. Martinez-Lamas), *stoucann@ifremer* (S. Toucanne)

ABSTRACT

Offshore archives retrieved from marine/lacustrine environments receiving sediment from large river systems are valuable Quaternary continental records. In the present study, we reconstruct the Danube River activity at the end of the last glacial period based on sedimentological, mineralogical and geochemical analyses performed on long-piston cores from the north-west Black Sea margin. Our data suggest that the Danube River produced hyperpycnal floods throughout the *ca.* 33-17 ka period. Four main periods of enhanced Danube flood frequency, each of 1.5-3 kyr duration, are recorded at *ca.* 32.5-30.5 ka (equivalent to the first part of Heinrich Stadial -HS- 3), at *ca.* 29-27.5 ka (equivalent to Greenland Stadial 4), at *ca.* 25.3-23.8 ka (equivalent to HS 2) and at *ca.* 22.3-19 ka. Based on mineralogical and geochemical data, we relate these events to enhanced surface melting of the Alpine Ice Sheet (AIS) that covered ~50,000 km² of the Danube watershed at the Last Glacial Maximum (LGM). Our results suggest that (*i*) the AIS growth from the inner Alps to its LGM position in the northern Alpine foreland started from *ca.* 30.5 ka, ended no later than *ca.* 25.3 ka, and was interrupted by a melting episode *ca.* 29-27.5 ka; (*ii*) the AIS volume drastically decreased from *ca.* 22.3 to 19 ka, as soon as summer insolation energy at the AIS latitude increased; and (*iii*) HSs strongly impacted the AIS mass balance through enhanced summer surface melt. This, together with evidence of severely cool winters and the rapid expansion of sea ice in the North Atlantic, implies strong seasonality in continental Europe during stadials.

Keywords: Danube River, floods, hyperpycnites, Alpine Ice Sheet, Heinrich Stadials, seasonality, Black Sea.

1. INTRODUCTION

Fluvial landforms and sediments can be used to reconstruct past hydrological conditions since rivers are highly sensitive to environmental changes (Blum and Törnqvist, 2000; Macklin et al., 2012). Prominent examples from the British Isles (Macklin et al., 2005; Macklin and Lewin, 2003) and continental Europe (Busschers et al., 2007; Gábris and Nádor, 2007; Gibbard, 1988; Kasse et al., 2010; Macklin et al., 2006; Mol et al., 2000; Pastre et al., 2003; Starkel et al., 2015; Vandenberghe, 2002) point to the impact of Quaternary climate change on river system dynamics. However, the riverine archives are highly complex (*e.g.* spatially-dependant types and rates of sedimentation, hiatus and erosion, difficulties in dating; Blum and Törnqvist, 2000; Coulthard et al., 2005; Macklin and Lewin, 2003; Vandenberghe, 2003). Hence the use of sediment archives retrieved offshore of large river systems can provide complementary high-frequency sediment flux records resulting from river discharge and climate variability (Simpson and Castelltort, 2012). This has been demonstrated in various geographic and climatic settings (*e.g.* Bonneau et al., 2014; Covault et al., 2011; Goodbred and Kuehl, 2000; Revel et al., 2010), including the giant glaciated catchments of European rivers, *i.e.* the Channel River (Ménot et al., 2006; Toucanne et al., 2009; Zaragosi et al., 2001) and the Dniepr River (Soulet et al., 2013). These studies provided remarkable new insights into the paleohydrology of Europe during past glacial intervals as well as into the impact of the Fennoscandian Ice Sheet (FIS) in amplifying, pacing and driving regional and global climate changes (*e.g.* Boswell et al., 2019; Soulet et al., 2013; Toucanne et al., 2015).

It is well-known that the Black Sea received vast amounts of sediment and meltwater from the Alpine Ice Sheet (AIS) and FIS during glacial periods (Bahr et al., 2006; Gorlach et al., 2017; Grosswald, 1980; Major et al., 2006; Mangerud et al., 2004; Soulet et al., 2013, 2011a; Tudryn et al., 2016). The Red Layers (*e.g.* Bahr et al., 2006), deposited in the north-west Black Sea by the Dniepr River and the retreating FIS between *ca.* 17.2 and 15.7 ± 0.3 cal ka BP (Soulet et al., 2013), constitute a prominent example further highlighting the ability for ice-sheets to impact sediment routing systems down to the deep sea 'sink' (Jaeger and Koppes, 2016). By comparison, the impact of AIS fluctuation on the Danube River discharge and Black Sea sedimentary system has received much less attention. Yet, the entire north-east part of the AIS (~50,000 km²) drained into the Black Sea and sediment accumulated in the Danube delta (Giosan et al., 2006, 2005; Panin et al., 1983) and deep-sea fan (Constantinescu et al., 2015; Lericolais et al., 2013; Popescu et al., 2001; Wong et al., 1994) must have recorded Danube River activity and AIS fluctuations during the late Quaternary. Here, we

provide a continuous, high-resolution record of the Danube River discharge into the Black Sea 'Lake' at the end of the last glacial period (from *ca.* 33.5 ka) through the study of two sediment cores retrieved midway between the Danube delta and the Danube deep-sea fan (Fig. 1). Millennial-scale variability in sediment input and source observed in our multi-proxy records suggests rapid regional-scale glacier fluctuations in the north-eastern Alps over the course of the AIS to its maximum extent and during the deglaciation.

2. GEOLOGICAL AND ENVIRONMENTAL SETTINGS

2.1 The north-west Black Sea and the Danube sediment routing system

Since its opening during the Upper Cretaceous, the Black Sea basin acts as a large sediment catchment area that accumulated a thick sedimentary cover of ~19 km in its western margin. Since the Pliocene, a 2.5 to 3 km-thick prograding depositional wedge has been formed by Danube and Dniepr sedimentary supplies (de Leeuw et al., 2018; Nikishin et al., 2003). This geological feature, forming the wide north-west Black Sea continental shelf (<140-170 m water depth) and margin, is incised by numerous erosive canyons (Riboulot et al., 2017) including the Danube Canyon which deeply incises the shelf over 26 km down to -110 m water depth (Popescu et al., 2004) (Figs 1 and 2). The Danube Canyon has fed an extensive, deep depositional (turbidite) system (*i.e.* Danube deep-sea fan) at water depths greater than 2000 m (Lericolais et al., 2013; Popescu et al., 2001; Wong et al., 1994). It has been active during the last glacial period and until *ca.* 11.7 ka (Constantinescu et al., 2015) when the Black Sea was a giant freshwater lake and lowstand conditions (~90-120 m below the present sea level) dominated (Deuser, 1972; Lericolais et al., 2011; Ross et al., 1970; Ryan et al., 1997; Yanchilina et al., 2017). The Danube deep-sea fan thus represents the final sink of the Danube sediment routing system (Matenco and Andriessen, 2013) (Fig. 1), *i.e.* the integrated dynamical system connecting erosion in mountain catchments of western Central Europe to downstream deposition in the Black Sea.

The Danube River is the second longest river in Eurasia, with a length of 2,900 km from the Black Forest (Germany) to its delta (Romania) (Fig. 1), a drainage area of 801,000 km^2 and a modern sediment load estimated at 42-67 Mt per year (sediment yield: ~80 $t.km^2.yr^{-1}$). Today, it constitutes by far the main sediment source for the northern Black Sea considering the low sediment load, estimated to be less than 10 Mt per year in total, for the rivers Dniestr (sediment yield: ~30 $t.km^2.yr^{-1}$), Dniepr and Don (sediment yield: ≤5 $t.km^2.yr^{-1}$). This difference is due to the mountainous character of the Danube drainage area in comparison to

the lowlands-dominated Dniestr, Dniepr and Don watersheds (Milliman and Farnsworth, 2013; Milliman and Syvitski, 1992; Panin and Jipa, 2002; Sommerwerk, 2009). Indeed, the Danube River collects water and sediment from the mountainous areas of the northern and eastern Alps (up to 4,049 m high at Piz Bernina; Fig. 3), the Dinarides and the Carpathians (Fig. 1), mainly formed of Variscan metamorphic and magmatic basements and Mesozoic calcareous rocks (Asch et al., 2005). In detail, from its source to its mouth, the Danube River receives the following: on its right bank, the tributaries Iller, Inn, Enns, Drava and Sava, originating in the Alps and the Dinarides, as well as the Velika Morava flowing from the Balkans; and on its left bank, the major tributaries Morava, rising in the Bohemian Forest, and Tisza, originating in the Carpathians, and the Jiu, Olt, Siret and Prut rivers, with sources in the Carpathians (Garnier et al., 2002) (Fig. 1). In addition to the riverine material from the mountainous areas, the glacial loess deposits constitute a significant additional sediment supply to the Danube sediment load, especially in the Pannonian (Middle Danube) and Dacic (Lower Danube) basins (Marković et al., 2015).

2.2 Paleoenvironmental changes in the Danube drainage area

The loess and glacigenic sequences preserved in the Danube catchment provide information on the intensity of Alpine glaciations (Marković et al., 2015), with the first major glaciation in the Alps dating from Marine Isotope Stage (MIS) 22 (Muttoni et al., 2003). The (local) Last Glacial Maximum (LGM) in the Alps (Upper Würmian, MIS 2; Chaline and Jerz, 1984, Figs 1 and 3) lasted from not later than *ca.* 24 to 20-19 ka (*e.g.* Ivy-Ochs, 2015; Ivy-Ochs et al., 2008; Monegato et al., 2017), with glaciers extending tens of kilometers out onto forelands and coalescing into huge (Rhine, Isar/Loisach, Inn, Salzach and Traun, from west to east) piedmont lobes (up to 700 m in thickness) in the Molasse Basin, Upper Danube (Ivy-Ochs, 2015; van Husen, 2000) (Fig. 3). This time period is coeval with peak loess accumulation rates in the Panonnian Basin (Fitzsimmons et al., 2012) and the development of the Duttendorf loess sequence in the Salzach palaeoglacier area (Starnberger et al., 2011). Recent compilation of ^{10}Be surface exposure dating and radiocarbon ages demonstrate that if LGM glaciers vanished rapidly from the foreland at *ca.* 20-18 ka, the initiation of retreat from their maximum positions occurred as soon as *ca.* 24-22 ka (Ivy-Ochs, 2015; Ivy-Ochs et al., 2004; Reber et al., 2014). Note that the timing for the growth and demise of cirque and cirque-valley glaciers in the western and southern Carpathians mountains matches that recognized in the northern Alps (Makos et al., 2018, 2014, 2013; Reuther et al., 2007).

143 In contrast, little is known about pre-LGM ice fluctuations (Ivy-Ochs et al., 2008). The
144 Middle Würmian (MIS 4 and 3; Chaline and Jerz, 1984) is poorly preserved in the Alps due to
145 the excavation of valleys by the LGM ice advance soon after *ca.* 33-32 ka (*i.e.* onset of the
146 Upper Würmian, as redefined by Spötl et al., 2013). However, recent ^{10}Be data from the
147 western Alps and the Rivoli-Avigliana end-moraine system (northern Italy) yield a minimum
148 age of 41.2 ± 1.9 ka (MIS 3) for pre-LGM glacier advance(s) in the Pô Valley (Ivy-Ochs et
149 al., 2018). This age fits well with the deterioration of climatic conditions over the Alps after
150 *ca.* 45 ka (Heiri et al., 2014; Starnberger et al., 2013). These results, including recent ones
151 from the Berchtesgaden basin (Germany; Mayr et al., 2019), corroborate numerical
152 simulations suggesting that a highly dynamic ice-sheet occupied the inner-Alpine regions
153 throughout the last glacial period, with possible recurrent short-lived advances onto the
154 forelands well before the LGM (Seguinot et al., 2018).
155
156 **3. MATERIALS**
157
158 **3.1. Sediment cores**
159 This study focuses on the Calypso long-piston cores GAS-CS01 (44°05.1′N, 30°47.5′E) and
160 MD04-2790 (44°12.8′N, 30°59.6′E) retrieved from the north-west Black Sea margin (Figs 1
161 and 2; Table 1). Core GAS-CS01 (33.4 m long) was collected at 240 m water depth from the
162 shelf margin, ~40 km east of the Danube Canyon head, during the GHASS oceanographic
163 cruise (R/V Pourquoi Pas?; Ker and Riboulot, 2015). Core MD04-2790 (30.3 m long) is
164 located at 352 m water depth, ~19.6 km east of GAS-CS01. This core was collected during
165 the ASSEMBLAGE-1 cruise (R/V Marion Dufresne; Lericolais, 2004) and has been
166 extensively studied over the last few years for chronostratigraphical and paleoenvironmental
167 studies (*e.g.* Soulet et al., 2011a,b; Sanchi et al., 2014). Note that the length of cores GAS-
168 CS01 (this study) and MD04-2790 (Soulet et al., 2011a) has been corrected after removal of
169 coring gaps (corrected length of 32.1 and 27.8 m, respectively). Core depths discussed in this
170 study thus correspond to depth (cm, m) below sea floor (bsf), and corresponding depths (raw -
171 cm- versus -cmbsf-) are presented in Tables 2 and 3.
172
173 **3.2. Danube River and tributary samples**
174 In order to track paleoenvironmental changes in the Danube sediment routing system,
175 eighteen riverine sediments have been recovered from the Danube River and its tributaries to
176 compare their mineralogy with that of the GAS-CS01 core samples (Fig. 1; Table 3). Fine-

177 grained river sediments constitute the mineralogical diversity of catchment areas. As such
178 they can provide a reliable average mineralogical and geochemical composition of their
179 corresponding drainage basin (Chamley, 1989; Sionneau et al., 2008). Considering the
180 disproportionate role of mountains and glaciers in the erosion processes and the river
181 sediment yields (Hallet et al., 1996; Milliman and Syvitski, 1992; Comiti et al., 2019), we
182 mainly collected river sediments from tributaries draining the northern Alps (*e.g.* Iller, Inn;
183 n=5), the western Carpathians (*e.g.* Tisza, Morava; n=5) and the Dinarides (Sava and Velika
184 Morava rivers; n=2). Additional samples were collected along the Danube mainstream (n=6)
185 from Passau (Germany) to the Black Sea, near the confluence with the Tisza and Velika
186 Morava rivers. At every location where fine sediment was available, samples were collected
187 from fresh bank deposit.
188
189 **4. METHODS**
190
191 **4.1 Core-scale analyses**
192 The sedimentological analysis of GAS-CS01 is firstly based on visual description and X-ray
193 images that allow the recognition of the main sedimentary facies and sequences, and the
194 manual counting of laminae/beds (see Part 6.1; Fig. 4). 2D X-ray images were acquired with a
195 Geotek XCT system (Ifremer, Brest) from split core sections. Detailed identification of the
196 sedimentary facies was completed by hyperspectral reconstructed images. The hyperspectral
197 spectroscopy technique consists of combining reflectance spectroscopy and digital imaging. A
198 high-resolution digital image of a sediment core and a reflectance measurement for a specified
199 wavelength range are collected in each pixel of the digital image. The wavelength intervals at
200 which absorption features appear in their reflectance spectra are determined by the chemical
201 compounds (*e.g.* organic matter) and physical properties (*e.g.* grain size) of the sediments
202 (Debret et al., 2018; Jacq et al., 2019; Van Exem et al., 2019). In this study, we present high-
203 resolution reconstructed images (spatial resolution of ~61 µm/pixel) in order to highlight the
204 sedimentary features in GAS-CS01. Hyperspectral images were acquired at the University of
205 Rouen (France) using a Specim (Spectral Imaging Ltd.) sediment-core-scanning system in
206 combinations with a Specim PFD-xx-V10E camera (Specim Ltd., Finland) and OLES22.5
207 lens. These high-resolution images were acquired in the VNIR (Visible and Near InfraRed)
208 spectral range between 400 to 1000 nm. The colour obtained with the VNIR is a false
209 (highlighted) colour constructed after selecting three bands in the RGB system (697.94,
210 548.87 and 469.59 nm).

211 The bulk intensity of major elements for core GAS-CS01 was analysed using an Avaatech
212 XRF core-scanner (Ifremer, Brest). XRF data were collected every 1 cm along the entire core,
213 with a count time of 10 s, by setting the voltage to 10 kV (no filter) and 30 kV (Pd thick filter)
214 and the intensity to 600 mA and 1000 mA, respectively. Millimetre-scale analyses were also
215 conducted on some sections (30 s., 10-30 kV, 1000 mA) (Fig. 5).
216 The global mineralogy composition of GAS-CS01 sediments was determined by X-ray
217 diffractometry (XRD), using a D8 Advance BRUKER model, a device type Bragg-Brentano
218 equipped with a Cu X-ray tube, a primary Soller slit of 0.6 mm, a nine-position sample holder
219 and the VANTEC-1 Position Sensitive Detector with a nickel filter (Ni 0.5). Prior to analysis,
220 dried sediment powders were inserted into the sample holder, and flattened. Measurements
221 were made from 5 to 70° with a resolution of 0.01° lasting 1 s. The voltage and amperage
222 were set up to 40 kV and 30 mA, respectively.
223 The clay mineralogy composition of GAS-CS01 sediments was determined by X-ray
224 diffractometry (XRD), using a D2 PHASER BRUKER model, a Bragg-Brentano device type
225 equipped with a Cu X-ray tube, a primary Soller slit of 0.6 mm and the LYNXEYE Detector
226 with a nickel filter (Ni 0.5). In order to separate the clays from the rest of the matrix, the
227 sample undergoes several stages of preparation: various chemical treatments to eliminate
228 carbonates, iron oxides as well as the organic matter and a settling. Finally, these clays are
229 plated on an oriented glass slide which is analysed in three different ways: without treatment,
230 after saturation with ethylene glycol and after calcination at 490°C. Measurements were made
231 from 2 to 30° with a resolution of 0.02° lasting 1 s. The voltage and amperage were set to
232 30 kV and 10 mA, respectively. The illite crystallinity (ICr) index, or Kübler index (Kisch,
233 1991), was measured from XRD results. The illite crystallinity (°Δ2θ) is the full width at half
234 maximum (FWHM) determined from the illite peak at 10 Å (Chamley, 1989). The clay
235 mineralogy and the ICr of the riverine samples (n=18) were also determined.
236 Finally, the geographical provenance of the GAS-CS01 sediments was determined measuring
237 Nd isotopic ratios of fine-grained detrital fraction (n=14). The neodymium isotopic
238 composition (ε_{Nd}) of terrigenous sediment is a powerful tracer for geographical provenance
239 because the ε_{Nd} signature of detrital sediment is retained during continental weathering and
240 subsequent transport (Bayon et al., 2015; Goldstein and Jacobsen, 1988). We focus on the
241 <63 µm fraction because the meltwaters of ice margins predominantly transport the clay and
242 silt fractions of continental detritus (Boswell et al., 2018; Brown and Kennett, 1998). All bulk
243 samples were first treated to quantitatively remove any biogenic, authigenic and organic
244 compounds (Bayon et al., 2002) and residual detritial fractions were digested by alkaline

fusion prior to isolation of the Nd by ion-exchange chromatography (Bayon et al., 2009). Nd isotope measurements were performed on a Thermo Scientific Neptune MC-ICP-MS at the Pôle Spectrométrie Océan, Brest (France). Mass bias corrections on Nd were made with the exponential law, using $^{146}Nd/^{144}Nd = 0.7219$. Nd isotopic compositions were determined using sample-standard bracketing, by analysing an internal standard solution every two samples. Mass-bias corrected values for $^{143}Nd/^{144}Nd$ were normalized to a JNdi-1 value. Replicate analyses of the JNdi-1 standard solution during the course of this study gave $^{143}Nd/^{144}Nd = 0.512113 \pm 0.000013$ (2SD, n=28), in full agreement with the reference value (0.512115) of Tanaka et al. (2000), and corresponding to an external reproducibility of ~ ±0.25 ε-units, taken as the estimated uncertainty on our measurements. In this study, both measured $^{143}Nd/^{144}Nd$ ratios and literature data are reported in ε_{Nd} notation $[(^{143}Nd/^{144}Nd)_{sample}/(^{143}Nd/^{144}Nd)_{CHUR} - 1] \times 10^4$, using $(^{143}Nd/^{144}Nd)_{CHUR} = 0.512638$ (Jacobsen and Wasserburg, 1980). The ε_{Nd} dataset available in core MD04-2790 for the *ca.* 28-10 ka period (Soulet et al., 2013) was produced using this procedure.

4.2 Laminae-scale analyses

To characterize the sedimentary facies of core GAS-CS01, and the laminations in particular (see Part 6.1), we performed microscopic observations of 8 cm long thin-sections of impregnated sediments. The thin sections were prepared at the Université de Bordeaux (UMR EPOC) according to the protocol described in Zaragosi et al. (2006). The studied intervals were selected from well-preserved and representative sedimentary facies (Fig. 4). The thin sections were then used for geochemical characterization of the sediments via scanning electron microscopy (SEM) at Ifremer, using a Thermo Scientific Quanta 200 equipped with an OXFORD Instrument X-MAXN silicon drift detector energy-dispersive X-Ray spectrometer (detector size: 80 mm²). The thin sections were coated with a thin layer of carbon and X-ray EDS maps acquired on an area of about 300 mm² to investigate the microscale geochemical distribution/composition of the sediments. Each area is composed of over 30 fields (3.47 × 3.04 mm each) scanned with a resolution of 1024 × 896 pixels (1 pixel = 3.4 µm). Additionally, morphological analyses of lithic grains were performed through SEM (Quanta 200). The grains were deposited onto SEM sample holders covered with a gold layer, and the SEM images were obtained with the secondary electron detector mode and an accelerating voltage of 5.0 kV.

Finally, we performed a total of 398 grain-size analyses using a Malvern Mastersizer 3000 laser diffraction particle size analyser (0.1-2000 µm) coupled with a Hydro LV wet dispersant

unit. Ultrasonic dispersion (2 minutes) was conducted before analysis. The average resolution is 0.25 cm along the studied intervals.

5. AGE-DEPTH MODEL

Core chronologies based on radiocarbon dates are hampered in the Black Sea by unconstrained reservoir age (Guichard et al., 1993; Jones and Gagnon, 1994; Kwiecien et al., 2008; Soulet et al., 2011a, 2019). To circumvent the reservoir age issue, it is possible to reconstruct a meaningful environmental proxy from the core sediment and align it to a calendrically-dated reference record (*e.g.* Bard et al., 2004, 2013; Heaton et al., 2013; Skinner et al., 2010, 2020; Soulet et al., 2011a) in order to obtain the calendar age-depth model without using radiocarbon dates. Original calendar age-depth model of core MD04-2790 is based on the alignment approach (Soulet et al., 2011a): TEX86-derived Lake Surface Temperature (LST) reconstructed from MD04-2790 sediments was aligned to Hulu Cave $\delta^{18}O$ speleothem record (Wang et al., 2001). The GAS-CS01 calendar age-depth model is based on that of core MD04-2790, through the alignment of their respective XRF-Ca records (Fig. 5) which provided calendar ages at tie-points. The striking resemblance of XRF-Ca records confirms that the XRF Ca_{norm} is a basin-wide stratigraphic proxy in the Black Sea (Bahr et al., 2005, 2008; Kwiecien et al., 2008; Soulet et al., 2011a; Constantinescu et al., 2015). Original MD04-2790 age-depth model was performed until to the depth 1990 cmbsf (31.3 ka), corresponding to depth 1595 cmbsf in core GAS-CS01. Below, MD04-2790 LST record did not provide reliable tie-point compared to Hulu Cave record (Soulet et al., 2011a). Hence, below the depth 1990 cmbsf in MD04-2790 and the depth 1595 cmbsf in GAS-CS01, the chronology is based on radiocarbon dates (*Dreissena* sp. and bulk organic matter; Table 2). We implemented these chronological constraints (Supplementary Table S1 and S2) in Oxcal (Bronk Ramsey, 2001, 2008, 2009; Bronk Ramsey and Lee, 2013; Bronk Ramsey, 2017). As reservoir ages are unconstrained for this period, we applied a vague reservoir age correction following a uniform distribution spanning 0 to 5000 ^{14}C yrs correction. Oxcal codes and further details of the modelled age-depth models are available in Supplementary Online Material. We found that the base of both cores consistently dates back to ~33.5 ka (Supplementary Figs. S1 and S2).

6. RESULTS

313 **6.1 GAS-CS01 lithology**

314 The analysis of core GAS-CS01 shows the the classic regional lithological succession
315 consisting of the microlaminated coccolith ooze (MCO; 0-0.04 mbsf), the black-brown micro-
316 laminated sapropel (0.04-0.52 mbsf), and the carbonate-rich layers (down to 2.53 mbsf)
317 overlying the Red Layers (2.53-4.26 mbsf). Below the Red Layers down to the bottom
318 (32.1 mbsf), the GAS-CS01 lithology consists of even, parallel clastic rythmites. This
319 lithological succession, found from the north-west Black Sea upper slope (Bahr et al., 2005;
320 Major et al., 2002; Soulet et al., 2011a) to the Danube deep-sea fan (Constantinescu et al.,
321 2015), corresponds to 'marine' Unit I (MCO, <2,720 ± 160 cal a BP) and Unit II (sapropel,
322 deposited from 8,080 ± 250 cal a BP) and below, 'lacustrine' Unit III (glacial 'banded lutites')
323 described by Ross and Degens (1974). Consequently, the carbonate-rich silty clay is
324 interpreted as the upper part of the 'lacustrine' Unit III (Dean and Arthur, 2011). This
325 sediment deposited during the late glacial (including the Bølling-Allerød Interstadial and the
326 Younger Dryas cold event), from 15.7 ± 0.3 cal ka BP (upper part of the Red Layers; Soulet et
327 al., 2011a) and the Initial Marine Inflow *ca.* 9 ka (Soulet et al., 2011b). Based on the above,
328 core GAS-CS01 therefore consists of a very high-resolution record of the glacial (*sensu*
329 *stricto*, > 16 ka) 'lacustrine' Unit III (until *ca.* 33.5 ka; see Part 5 'Age-depth model').
330 In detail, the glacial sequence of GAS-CS01 is fully laminated (total of 3815 laminae/beds
331 revealed by X-ray imagery) and consists of even, parallel clastic rhytmites that resemble the
332 varve pattern of Degens et al. (1978). They consist of silty to sandy graded deposits, evolving
333 gradually from millimetre- (*i.e.* laminae; Scandinavian-type lacustrine varves of Degens et al.,
334 1978) to decimetre-thick deposits (*i.e.* beds; megavarves of Degens et al., 1978) from the Red
335 Layers (2.53-4.26 mbsf) to the core bottom (32.1 mbsf) (Figs 4 and 6). They are separated by
336 muddy intervals of similar thickness (*i.e.* mm- to dm-thick from top to bottom). Interestingly,
337 the grain-size of the deposits is positively correlated with the thickness of the clastic intervals,
338 from silt-sized grains in the Red Layers to sand-sized particles in the deeper part of GAS-
339 CS01. High-resolution grain-size analyses reveal the superposition of (basal) coarsening-up
340 and (top) fining-up sequences throughout GAS-CS01. This pattern is mirrored by the
341 millimetre-scale XRF Zr/Rb, well-known as a semi-quantitative grain-size indicator (Dypvik
342 and Harris, 2001) (Figs 7, 8 and 9). All these results (and the inversely graded facies in
343 particular) suggest that the clastic rhytmites in GAS-CS01 are hyperpycnite sequences, *i.e.*
344 deposits that are related to quasi-steady hyperpycnal (*i.e.* 'above a density threshold')
345 turbidity currents (Mulder et al., 2003; Mulder and Alexander, 2001). The detailed
346 observation of X-ray images and thin-sections reveal similar sedimentary deposits (including

4841 laminae) at site MD04-2790 (Soulet et al., 2011a), ~20 km east of GAS-CS01. This highlights the regional imprint of hyperpycnal flows in the north-west Black Sea 'Lake' during the last glacial period.

6.2 Hyperpycnal turbidites frequency

The frequency of hyperpycnal turbidite deposits (hyp.250 yr^{-1}) has been estimated for cores GAS-CS01 and MD04-2790 (Fig. 10b and Supplementary Online Material). The two cores present similar trends. A peak in hyperpycnal turbidite frequency (>100 hyp.250 yr^{-1}) is observed from *ca.* 32.5-30.5 ka with a maximum (up to 380 hyp.250 yr^{-1} at GAS-CS01) estimated at *ca.* 31 ka. A rapid decrease is observed thereafter (<50 hyp.250 yr^{-1}), followed by a new increase centred at 29-27.5 ka (~150 hyp.250 yr^{-1} at MD04-2790). Then, a ~10-kyr-long period (from *ca.* 27 to 17 ka) of moderate hyperpycnal turbidite frequency fluctuating between ~15 and 50 hyp.250 yr^{-1} is observed. During this interval, two main episodes of increasing frequency (up to ~50-70 hyp.250 yr^{-1}) are observed, at *ca.* 25.3-23.8 ka and at *ca.* 22.3-19 ka. A last peak in hyperpycnal turbidite frequency is observed at the two sites at 17.2- 16 ka, *i.e.* during the deposition of the Red Layers. The evolution of sediment accumulation rates calculated for the two cores strictly follows that of the hyperpycnal turbidite frequency (Fig. 10c).

6.3 Sedimentary geochemistry

6.3.1 Clay mineralogy

The GAS-CS01 clay mineralogy (n=146; Fig. 10d,e and Supplementary Online Material) reveals the dominance of both smectite (39 ± 13%) and illite (36 ± 10%) over chlorite (15 ± 7%) and kaolinite (11 ± 5%). From *ca.* 31 to 17.2 ka, the abundance of clay minerals fluctuates (up to ~15-20% variability for smectite) but is relatively stable in comparison to the >31 ka (peak in hyperpycnal turbidite frequency; see Part 6.2) and <17.2 ka (Red Layers) intervals. Indeed, the oldest interval of GAS-CS01 is characterised by high abundances in illite (~40-45%) and chlorite (~20-30%), but low abundances in smectite (~30%) and kaolinite (~5-10%), in comparison to the subsequent *ca.* 31-17.2 ka interval. Similarly, the smectite content abruptly decreases from *ca.* 17.2 ka (<10%) while the content in kaolinite (up to 25%) and illite (up to 60-70%) significantly increases. Note that despite a general low abundance, kaolinite is the only clay mineral to show a distinct signature for the three time periods considered.

The Danube River tributary samples (n=12) were divided into three groups corresponding to the north-eastern Alps (n=5), the Carpathians (n=5) and the Dinarides (n=2) mountainous areas (Table 3). River samples from the Alps show an illite content of ~40-50% while chlorite represents ~25% of the clayey fractions. Kaolinite and smectite contents are low, usually <5%, except in the Iller River where the smectite content reaches 40%. Smectite (~55%) dominates over illite (~25-30%) in the Carpathians, while an inverse pattern is observed in the Dinarides (~45-50% and ~20-25% of illite and smectite, respectively). The clay mineralogy of these zones contrasts with that of the north-eastern Alps with significant abundance of kaolinite (~10-20%) and very low content of dolomite (<2%). Dolomite abundance is significant (up to 17%) in the Alpine rivers.

6.3.2 Illite crystallinity index

The illite crystallinity index (ICr) in GAS-CS01 (n=146) shows values ranging from ~0.25° at the core bottom to ~0.60° in the Red Layers interval (Fig. 10f and Supplementary Online Material). In between, the ICr values range from ~0.30° to 0.40°. The increase in ICr values in the Red Layers is abrupt (at *ca.* 17.2 ka). In contrast, the ICr decreases gradually from *ca.* 33.5 ka to *ca.* 30 ka.

The ICr values of the Danube tributary river samples (n=12) are more homogeneous than in core GAS-CS01. ICr values reach a maximum of only 0.34-0.39° in the northern Alps (Iller River and the Danube at Passau). The ICr minimum (0.20°) is found in the (upper) Drava River sample, eastern Alps (Table 3).

6.3.3 ε_{Nd}

The ε_{Nd} dataset used in this study is from core MD04-2790 (n=84) for the *ca.* 28-10 ka period (Soulet et al., 2013) and from core GAS-CS01 (n=14) for the *ca.* 32-28 ka period (Fig. 10g). GAS-CS01 sediment show an ε_{Nd} value of -11.0 at *ca.* 28 ka, in line with the ε_{Nd} signature of -11.3 ± 0.3 (n=53) for the glacial MD04-2790 sediment (except Red Layers, see the discussion below). ε_{Nd} values gradually change towards the core bottom, reaching about -9.4 ± 0.1 (n=9) over the *ca.* 33.5-31 ka period (Supplementary Online Material).

7. DISCUSSION

7.1 Linking GAS-CS01 and MD04-2790 sedimentary sequences to Central European rivers

7.1.1 Sedimentological evidence for direct connection between Central European sediment sources and Black Sea depositional sinks

The sedimentological investigation of core GAS-CS01 shows that the continuous, rhythmic layering observed throughout the core (Fig. 4) consists in the succession of coarsening-upward and fining-upward units characteristics of hyperpycnal turbidity-current deposits (*i.e.* hyperpycnites; Mulder et al., 2003), at both the decimetre (lower part of GAS-CS01; Fig. 7) and millimetre scales (upper part of the core; Fig. 9). Thus, we attribute each clastic rhythmite (laminae or beds; Fig. 4) in GAS-CS01 to a discrete hyperpycnal flow. Hyperpycnal flows are defined as a bottom-riding flow evolving from a hyperpycnal plume, which descends to the basin floor as a result of excess density generated by its sediment load. Hyperpycnal flows are thus seen as the continuation of river discharges (*i.e.* floods) in subaqueous environments (Mulder et al., 2003, 1998; Mulder and Syvitski, 1995; Normark and Piper, 1991; Piper and Normark, 2009). They are frequent in freshwater lakes where only small particle density thresholds are necessary to trigger plunging (Mulder et al., 2003). The brackish water conditions prevailing in the Black Sea during the last glacial period (Deuser, 1972; Marret et al., 2009; Ross et al., 1970; Schumilovskikh et al., 2014; Soulet et al., 2010; Wegwerth et al., 2016), combined with the increased surface runoff and sediment load of the western Black Sea rivers (*e.g.* Danube, Dniepr) due to the combination of reduced vegetation cover and widespread permafrost (Kasse et al., 2010; Sidorchuk et al., 2011, 2008) likely favoured the generation of hyperpycnal flows and their deposits at the GAS-CS01 site. The recording of these events, and by extension of the river floods, was also favoured by the proximity to the GAS-CS01 site and the delta of the western Black Sea rivers. Indeed, the glacial lowstand conditions (lake level ~90-120 m below the present sea level; Figs 1 and 2) significantly reduced the river mouth distance to the shelf margin. This evidence suggests that the 3815 hyperpycnites of core GAS-CS01 provides a high-resolution flood record in the north-west Black Sea over the *ca.* 33.5-15 ka interval. Similarities in both the stratigraphy (see the XRF Ca_{norm} for a prominent example; Fig 5) and sedimentology (*i.e.* rhythmic layering throughout; Fig. 6) observed in core MD04-2790 (Soulet et al., 2011a), ~20 km east of GAS-CS01, highlights the regional imprint of river floods in the north-western part of the glacial Black Sea 'Lake'.

Reconstructed hyperpycnite frequency indicates that both GAS-CS01 and MD04-2790 sites experienced five main periods of increased flood frequency (F_x), each of 1.5-3 kyr duration, over the *ca.* 33.5-15 ka interval. These periods occurred simultaneously at both sites, at

449 *ca.* 32.5-30.5 ka (F_5), corresponding to the peak maximum, and at *ca.* 29-27.5 ka (F_4),
450 *ca.* 25.3-23.8 ka (F_3), *ca.* 22.3-19 ka (F_2) and *ca.* 17.2-15.7 ka (F_1) (Fig. 10b,c). The
451 simultaneity of each of the F_x periods at sites GAS-CS01 and MD04-2790 importantly
452 suggests a common forcing and, potentially, a unique river source at the two sites. This is
453 fittingly demonstrated for the F_1 period, *ca.* 17.2-15.7 ka. Geochemical investigations of
454 MD04-2790 sediment and the use of neodymium isotopic composition show that the sediment
455 composing the Red Layers originated from the decaying FIS and were transported to the
456 Black Sea by the Dniepr River (Soulet et al., 2013). Thus, the F_1 peak in GAS-CS01 and
457 MD04-2790 result from the increase in the frequency of hyperpycnal flows generated at the
458 Dniepr River mouth in response to ice mass fluctuations ~1,200 km northward (Fig. 1; Soulet
459 et al., 2013). The available geochemical dataset reveals that the unique, major river source for
460 hyperpycnal flows over the *ca.* 33.5-17.2 ka interval and the F_2, F_3, F_4 and F_5 peaks was the
461 Danube River (see Part 7.1.2). The concomitance between climate, sediment input and
462 geochemical signature changes (smectite abundance, ε_{Nd}, etc.; Fig. 10) excludes both an
463 autogenic origin (*i.e.* internally generated 'noise') and lake-level changes (highly debated over
464 the last glacial period; see Lericolais et al., 2011 and Vidal et al., 2010 for contrasting
465 conclusions) for the observed variability in the sedimentary record at the GAS-CS01 and
466 MD04-2790 sites (see Part 7.2).
467
468 **7.1.2 Deciphering river sources**
469 7.1.2.1 Neodymium isotopic composition
470 The sediment of the Red Layers deposited between *ca.* 17.2 and 15.7 ka (F_1 peak) are
471 characterised by ε_{Nd} values of -14.5 ± 1.3 (down to -18; n=24; Soulet et al., 2013). These
472 values are close to ε_{Nd} values of sediments of the Baltic area (Boswell et al., 2019, 2018;
473 Soulet et al., 2013; Toucanne et al., 2015) and the rivers Dniepr (ε_{Nd} of -14; Soulet et al.,
474 2013) and Don (-14.3, this study) showing that the Red Layer sediments originated from the
475 decaying FIS (Soulet et al., 2013). In contrast, the glacial sediment in MD04-2790, from
476 *ca.* 28 ka (oldest ε_{Nd} analysis in Soulet et al., 2013) to 11.7 ka shows homogenous but very
477 distinct ε_{Nd} values of -11.3 ± 0.3 (n=53). The latter signature is close to that of the European
478 Alps (Soulet et al., 2013), for which the northern and eastern parts (sediment yield of 160 and
479 220 $t.km^2.yr^{-1}$, respectively; Hinderer et al., 2013) represent a substantial contribution to the
480 Danube sediment discharge (mean sediment yield: 83 $t.km^2.yr^{-1}$). Indeed, Alpine rivers carry
481 fine-grained sediments with modern ε_{Nd} values ranging from about -10.8 for the Pô River

(south-western Alps; Frost et al., 1986), -10.2 ± 0.5 for the Rhône River (western Alps; Henry et al., 1994) and -9 for the Rhine (north-western Alps; Bayon et al., 2015) and the Danube (north-eastern Alps) rivers (Soulet et al., 2013). The Nd isotopic values of these Alpine rivers match those of the Quaternary loess of the Carpathian Basin (-10.4 ± 0.6, *n*=20; Újvári et al., 2012). Based on the above, we thus assume that the glacial ε_{Nd} signatures of -11.3 ± 0.3 at site MD04-2790 are mainly ascribed to the Alps-Carpathian realm and, by extension, to the Danube River. Nevertheless, it cannot be ruled out that a slight contribution from the Dniepr and Don (ε_{Nd} of about -14) at the studied sites possibly lowered the 'pure' ε_{Nd} signature (-11/-9) of the Danube to its lower (*i.e.* unradiogenic) end members during the last glacial period. This mixing is supported by the significant increase in ε_{Nd} at *ca.* 33-31 ka (F_5 peak), with radiogenic values (about -9) that undoubtedly excludes all river sources except that of the Danube at that time.

7.1.2.2 Clay mineralogy and illite crystallinity

Illite and smectite dominates the clay mineralogy of GAS-CS01 sediment (Fig. 10d). Illite is a good marker for northern river sources in the Black Sea (Stoffers and Müller, 1978; Tudryn et al., 2016), including the Danube River (Table 3), but it shows a maximal abundance (>40%) both during the 'non-radiogenic' Dniepr-sourced F_1 peak (*i.e.* Red Layers; ε_{Nd} down to -18) and the 'radiogenic' Danube-sourced F_5 peak (ε_{Nd} about -9). Thus, it cannot be used to decipher sediment sources in the north-west Black Sea. The combination of illite with kaolinite at GAS-CS01 during the F_1 peak is a peculiar mineralogical signature over the studied interval. Illite and kaolinite are typical of (paleo)soils, pedogenic processes and long-term weathering of sedimentary basins (Chamley, 1989) and appear as the main clay minerals in the Volga and Dniepr-Donets basins (Makshaev and Svitoch, 2016; Misch et al., 2018; Vishnevskaya and Sedaeva, 2000), thus supporting an eastern Central European origin for the deposition of Red Layers (Soulet et al., 2013). On the other hand, the low kaolinite content (~5-15%), together with the ε_{Nd} values, exclude this source (at least as a major contributor) for glacial sediment input to the margin between *ca.* 33.5 and 17.2 ka.

Smectite content is low to absent in the Red Layers but represents 30 to 60% of the *ca.* 33.5-17.2 ka interval at GAS-CS01. Smectite is well-represented in the Danube drainage basin (Tudryn et al., 2016), particularly in the Dinarides (~20-25%) and the Carpathians (~45-55%; Table 3). In the latter region, it probably originates from chemical hydrothermal weathering of volcanic rocks (Chamley, 1989), as shown in the Tisza basin (*e.g.* Tokaj Mountains and the

Calimani-Gurghiu-Hargita volcanic chain in the northern and eastern Carpathians, respectively; Bobos, 2012; Kiss et al., 2010). In the Alpine domain of the Danube, smectite is restricted to the western part of the Molasse Basin as shown by mineralogical data from the Iller River (40%; Table 3) and the neighbouring Lake Constance (Müller and Quakernaat, 1969). It is important to note that the Rhine glacier covered Lake Constance during the last glacial period and drained into the Danube (Ellwanger et al., 2011), thus providing a significant source of Alpine smectite, with chlorite and dolomite (Müller and Quakernaat, 1969; Schmieder et al., 2004), to the north-west Black Sea. Chlorite content is also significant (~25-30%) in the Alpine domain, in rivers draining both the northern (*e.g.* Inn, Enns) and central eastern Alps (*i.e.* eastern Dolomites and the Drava River; Table 3), where physical weathering at high altitudes dominates (Chamley, 1989; Müller and Quakernaat, 1969). Chlorite content in GAS-CS01 reaches a maximum (~25%) during the F_5 peak together with an increase in dolomite (~10%), a common mineral in the inner Alps (Upper Rhine, Iller, Enns, Drava; Table 3). Thus, the mineralogical signature for the F_5 peak suggests a significant Alpine contribution. More generally, these data together with ε_{Nd} support our contention that the Danube River was the main source for sediment input to the margin over the *ca.* 33.5-17.2 ka interval.

This is further supported by the ICr values of 0.32 ± 0.04 at GAS-CS01 (Fig. 10f) that fit well with those obtained for the Danube river samples (0.3 ± 0.05; Table 3). Such values are indicative of illite formation in low-grade metamorphic, high anchizonal conditions (*i.e.* lower greenschist facies; Kubler, 1967), typical of the central and eastern Alps (Bousquet et al., 2008; Krumm et al., 1988; Rantitsch, 1997; Schramm, 1991), the Dinarides (Rainer et al., 2002) and the Carpathians (Árkai, 1991; Árkai et al., 2003; Ciulavu et al., 2008). Interestingly, the F_5 peak shows ICr values down to 0.23° pointing to anchizonal-epizonal thermal conditions (*i.e.* blueschist facies). Such metamorphic conditions are restricted to the western (Gemer and Bükk units; Árkai, 1991) and southern parts (Danubian window; Ciulavu et al., 2008) of the Carpathians, and the Engadine (up to 4,049 m at Piz Bernina) and Taeurn (up to 3,898 m at Grossglockner) windows of the eastern and central Alps, respectively (Bousquet et al., 2008; Nievergelt et al., 1996; Schramm, 1991) (Figs 1 and 3). The dolomite enrichment at *ca.* 33-31 ka together with the above ICr values, points to these high alpine sources for the F_5 peak sediments, and by extension to the Drava (and its tributaries; *e.g.* Mur), that drain both the Dolomites and the southern Taeurn window, and the Inn rivers. The Inn River has its source in the Bergell Massif (upper Engadine valley) and the Salzach River, its main tributary, drained the northern part of the Tauern window (Fig. 3). Interestingly, the

549 ε_{Nd} values of the F_5 peak (-9.4 ± 0.1, *n*=9) match with the lower range of ε_{Nd} values (-
550 8.0 ± 1.4, *n*=9) determined for recent granites in the high Central Alps, including the Bergell
551 Massif (Juteau et al., 1986). Altogether, the neodymium isotopic composition, the clay
552 mineralogy and the ICr highlight the imprint of the Danube River on the north-west Black Sea
553 margin sedimentation during the *ca.* 33.5-17.2 ka interval.
554 The above finding is in line with geomorphological aspects from the continent interior to the
555 deep Black Sea. First, the modern contribution of the 'mountainous' Danube to the Black Sea
556 exceeds that of the 'lowlands' Dniester, Dnieper and Don by a factor 8 (see Part 2.1; Milliman
557 and Farnsworth, 2013; Milliman and Syvitski, 1992; Panin and Jipa, 2002), and this
558 difference was strongly enhanced during the last glacial period by the presence of the AIS and
559 Carpathian glaciers in the Danube drainage area (see Part 2.2). In contrast, the southern limb
560 of the FIS entered the Upper Dniepr basin only during a short period *ca.* 20-17 ka (Hughes et
561 al., 2016; Karabanov and Matveyev, 2011; Soulet et al., 2013) (Fig. 1). Moreover, the
562 physiography of the shelf-penetrating Danube Canyon (Popescu et al., 2004) and the high
563 sediment inputs into the Danube deep-sea fan (Constantinescu et al., 2015) are indicative of
564 both a high Danube sediment discharge and of a good connectivity between the Danube delta
565 and the shelf margin where cores GAS-CS01 and MD04-2790 are located (Fig. 2). As such,
566 the physiography of the margin suggests that the GAS-CS01 site was located at only ~20-
567 30 km (~50 km for MD04-2790) from the Danube paleo-delta front (~130 km today) during
568 glacial lowstand conditions (Popescu et al., 2004). Sediments deposited at sites GAS-CS01
569 and MD04-2790 between *ca.* 33.5 and 17.2 ka therefore record the evolution of the Danube
570 basin.
571
572 **7.2 From the Black Sea sedimentary record to the Alpine Ice Sheet**
573
574 The above geochemical constraints, together with the timing for the F_5 (*ca.* 32.5-30.5 ka), F_4
575 (*ca.* 29-27.5 ka), F_3 (*ca.* 25.3-23.8 ka) and F_2 (*ca.* 22.3 to 19 ka) peaks, suggest increased
576 Danube sediment discharges during Heinrich Stadial (HS; *i.e.* a stadial which contains a
577 Heinrich event as defined by Sanchez Goñi and Harrison, 2010) 3 (*ca.* 32-29 ka), Greenland
578 Stadial 4 (*ca.* 28.6-27.8 ka), HS 2 (*ca.* 26-23.5 ka) and during the period corresponding to the
579 transition from the global LGM to the Northern Hemisphere deglaciation, respectively. This
580 correlation highlights a close relationship between Danube River flood frequency and climate
581 change. Nowadays, severe floods in the Alpine-Carpathian range are triggered by heavy, late
582 spring to fall precipitation (*e.g.* Blöschl et al., 2013; Parajka et al., 2010). Holocene

583 reconstructions of the flood frequency in the central and north-eastern Alps reveal centennial-
584 to millennial-scale fluctuations in flood activity, with high flood activity correlated with cool
585 periods (lows in solar activity, global/alpine glacier advances; Glur et al., 2013; Swierczynski
586 et al., 2013; Wirth et al., 2013).
587 During the last glacial period, the continental ice build-up promoted cooling and enhanced
588 aridity over Europe (Wu et al., 2007). Precipitation over the Alps and Carpathians occurred
589 mainly in the form of snow. This inhibited the generation of floods from high-altitude sites,
590 but participated in the build-up of glaciers over the Carpathians and of the AIS during the last
591 glacial period (Figs 1 and 3). The AIS built up, reached its glacial maximum extent (covering
592 up to ~50,000 km^2 of the Danube watershed) and thickness (up to 2,500 m in the Hohe Tauern
593 region; Figs 3 and 11), and eventually shrunk over the *ca.* 33-17.2 ka interval (*e.g.* Ivy-Ochs,
594 2015; Ivy-Ochs et al., 2008; Seguinot et al., 2018). Pullback of glaciers from their maximum
595 extent (*i.e.* Alpine LGM) was underway by *ca.* 24-22 ka, and glaciers had receded within the
596 mountain front by *ca.* 19-18 ka (*e.g.* Ivy-Ochs, 2015; Monegato et al., 2017; Reitner, 2007).
597 This has been widely documented in the north-eastern Alps, including the Rhine, Iller, Isar,
598 Loisach, Inn, Salzach, Enns and Drava valleys (Ellwanger et al., 2011; Habbe and Rögner,
599 1989; Heiri et al., 2014; Ivy-Ochs et al., 2008; Preusser, 2004; Reitner, 2012; Spötl et al.,
600 2013; Starnberger et al., 2009; Van Husen, 2004). Thus, glaciers retreat must have supplied
601 meltwater and sediment to the to the Danube sediment routing system.
602 The timing for the Alpine (and Carpathian; Makos et al., 2018, 2013) deglaciation closely
603 matches that of enhanced Danube river floods from *ca.* 22 to 19 ka (F_2 peak). This strongly
604 suggests that the F_2 peak originated from the rapid downstream transport of glacigenic
605 sediments by AIS (and possibly Carpathian glaciers) meltwater, an assumption supported by
606 the glacigenic character of the lithic grains found in GAS-CS01 (Supplementary Fig. S3).
607 Onshore ice retreat and concomitant offshore sediment pulse is a common feature of large-
608 scale glaciated sediment routing systems (*e.g.* Mississippi in North America, Kolla and
609 Perlmutter, 1993; Channel River, Rhine, Rhone or Po in Europe, Bonneau et al., 2017;
610 Hinderer, 2001; Pellegrini et al., 2017; Toucanne et al., 2010). In these systems, sediment
611 production greatly exceeds transport capacity, hence downstream release of sediments occurs
612 through pulses of meltwater floods when glaciers retreat. Thus, the F_2 peak (sourced by the
613 AIS-Danube system) as well as the F_1 peak (sourced by the FIS-Dniepr system; Soulet et al.,
614 2013) share the common genetic origin of ice melting. Together with the geochemical results,
615 we thus suggest that the F_5 (*ca.* 32.5-30.5 ka), F_4 (*ca.* 29-27.5 ka) and F_3 (*ca.* 25.3-23.8 ka)

peaks, just like F_2, were triggered by significant ice melting and meltwater production in the Danube basin.

Little is known about ice fluctuation in the Alps before the deglaciation (*e.g.* Ivy-Ochs et al., 2008). The Tagliamento end moraine system of the south-eastern Alps (Fig. 3) provides insights into AIS fluctuations at the LGM. Two phases of glacial culmination occurred from 26.5 ka and at *ca.* 23-21 ka, separated by a distinct recession which ended no later than *ca.* 23 ka (Monegato et al., 2017) (Fig. 12e). This recession, also recognized in the neighbouring Brenta glacier region (Rossato and Mozzi, 2016; Fig. 3), is concomitant with enhanced Danube river floods and the F_3 peak, while the two glacier advances are coeval with the minima in the Danube River discharge at *ca.* 27-25.3 ka and from *ca.* 23.8 ka (Fig. 12b). The Tagliamento and Brenta glaciers were draining south into the Adriatic, suggesting that the timing of ice fluctuations in the Danube basin was similar to that of the south-eastern Alps with a significant melting episode at *ca.* 25.3-23.8 ka (F_3 peak). The hypothesis is supported by the fact that both the Tagliamento and Brenta glaciers in the south-eastern Alps, and the Inn, Salzach, Traun, Mur and Drava glaciers in the Danube basin were all draining the Hohe Tauern region and the Engadine ice dome in the central eastern Alps (Florineth and Schlüchter, 2000; Seguinot et al., 2018; Fig. 3). Geochemical data characterizing the GAS-CS01 sediment during F_5 peak (high ε_{Nd} and dolomite content, and low ICr; see Part 7.1 and Fig. 10) also suggest this region as the source of sediment.

F_5 peak in hyperpycnal flow frequency suggests a significant retreat of the AIS at *ca.* 32.5-30.5 ka, with significant remobilization (via meltwater) of the glacigenic sediment from the Engadine (*e.g.* upper Inn) and Tauern (*e.g.* upper Salzach and Drava) valleys. By extension, this indicates that ice caps were mainly restricted to the high Central Alps before *ca.* 32 ka, with a configuration that could resemble that proposed in Figure 11. This is consistent with the radiocarbon chronology of the Inn Valley that indicates that glaciers were upstream of (but close to) the Innsbruck region (*i.e.* ~100 km of the Alpine foreland) *ca.* 33-32 ka (Spötl et al., 2013). It is noteworthy that the sediment flux at the GAS-CS01 and MD04-2790 sites was greater during the F_5 peak than during the F_2, F_3, and F_4 peaks. The amplitude of the F_5 peak could be explained by very low lake-level conditions, basinward migration of the Danube delta or even lateral changes in sediment dispersal and depocenter considering the fact that the F_5 peak is higher at site GAS-CS01 than at site MD04-2790 (Fig. 10). However, these forcings alone cannot explain the alpine geochemical signature (*i.e.* high Central Alps) observed at that time. As a result, we propose that the F_5 peak (as well as the F_4 peak, see below) is the result of a short term glacier retreat event that occurred in the course of the

650 longer term growing phase of the AIS toward its LGM extent. Resulting pulse in meltwater
651 flood flushed a huge amount of glacigenic material (*i.e.* no longer available) accumulated in
652 the high Alps since the previous glaciation (MIS 4 or even before; Ivy-Ochs et al., 2008; van
653 Husen, 2000). In addition, our results suggest that the rapid ice growth that led to the invasion
654 of the northern Alpine foreland by the major AIS ice-streams at the LGM started after
655 *ca.* 30.5 ka, *i.e.* after the retreat interval mirrored by the F_5 peak, and ended no later than
656 *ca.* 25.3 ka (onset of the F_3 peak). Such timing is consistent with that reported for the western
657 Carpathians (Makos et al., 2018) and the northern foreland of the Swiss Alps (*e.g.* Rhine
658 glacier; Preusser et al., 2011) (Fig. 12d). Finally, the F_4 peak suggests that the LGM ice
659 advance was interrupted (with glaciers melting in the north-eastern Alps) between *ca.* 29 and
660 27.5 ka. Our results imply that the ice front in the Inn Valley (Spötl et al., 2013) advanced to
661 its LGM position at a rate of about 20-45 m/year (~100 km in a maximum of 2,200-5,200
662 years).
663 This rapid change in AIS volume and extent modified the regional pattern of erosion (*e.g.* Jiao
664 et al., 2018), which may explain the mineralogical changes observed at the GAS-CS01 site
665 after the F_5 peak. This includes in particular the dominance of smectite in clay assemblages
666 (Fig. 10d) and the disappearance of the signature (ICr, ε_{Nd}; Fig. 10f,g) of the Engadine and
667 Tauern source areas. These two regions were rapidly covered by ice (>1 km in thickness at the
668 LGM; Florineth and Schlüchter, 2000) and the sediment-laden meltwater reaching the north-
669 west Black Sea then mainly originated from the ice-streams located in the northern Alpine
670 foreland, including those of the Rhine (Ellwanger et al., 2011) and the Iller valleys (Habbe
671 and Rögner, 1989) that remobilize smectite-rich sediments (Müller and Quakernaat, 1969;
672 Table 3) (Fig. 11).
673 It is striking how Danube River flood activity *ca.* 33-17 ka closely resembles that of the Po
674 River, Italy (Fig. 12c). Indeed, the F_5, F_4, F_3 and F_2 Danube peaks are coeval with rapid
675 increases in sediment flux (up to 200 km^3/kyr) in the Po delta, which accumulated ~350 m of
676 sediment from the southern AIS *ca.* 32-14 ka (Pellegrini et al., 2018, 2017). This result
677 indicates that the sediment flux of the Danube and Po rivers was not controlled by basin base
678 level changes (*i.e.* water-level fluctuations) because they evolved independently in the
679 Mediterranean and Black Seas during glacial periods (Badertscher et al., 2011). Hence, AIS
680 mass-balance changes must explain the similar sediment flux pattern observed offshore of the
681 Po and Danube rivers during glacial times. The close resemblance between AIS fluctuations
682 in the Danube catchment and the regional precipitation pattern (*i.e.* 7H $\delta^{18}O$ record of the

683 Sieben cave system; Luetscher et al., 2015), that partly controlled glacier mass balance
684 (Fig. 12d), suggests that the AIS as a whole was responding to large-scale climate forcing.
685
686 **7.3 Enhanced surface melting of the Alpine Ice Sheet during periods of North Atlantic**
687 **cooling**
688
689 In the above discussion, we have showed that the F_5 (*ca.* 32.5-30.5 ka), F_4 (*ca.* 29-27.5 ka), F_3
690 (*ca.* 25.3-23.8 ka) and F_2 (*ca.* 22.3 to 19 ka) peaks in hyperpycnal flow frequency, resulting
691 from increased Danube sediment discharges, likely resulted from enhanced surface melting of
692 the AIS during HS 3 (*ca.* 32-29 ka), Greenland Stadial 4 (*ca.* 28.6-27.8 ka), HS 2 (*ca.* 26-
693 23.5 ka) and the very end of the global LGM. The timing of these episodes of AIS melting has
694 important implications, at regional to continental scales. The last episode of AIS melting
695 recorded in this study (*i.e.* F_2 peak in the Danube record, and its equivalent in the Po delta)
696 occurred *ca.* 22-19 ka. This time interval corresponds to the onset of the widespread retreat of
697 the Northern Hemisphere ice sheets in response to high northern latitude summer insolation
698 forcing (Carlson and Clark, 2012; Clark et al., 2009). This event is well-documented for the
699 FIS that rapidly retreated in the Baltic lowlands at that time (Hughes et al., 2016; Larsen et al.,
700 2009; Stroeven et al., 2016; Toucanne et al., 2015, 2010). In contrast, the rapid acceleration in
701 the FIS retreat from *ca.* 18 ka (HS 1; Hughes et al., 2016; Toucanne et al., 2015, 2010;
702 Zaragosi et al., 2001) has no AIS equivalent in the north-west Danube and Po sedimentary
703 records. Sediment flushed by AIS fluctuations younger than *ca.* 19 ka (*i.e.* Alpine Lateglacial,
704 including the Gschnitz stadial *ca.* 17-16 ka; Ivy-Ochs, 2015) could have been trapped in
705 glacier-shaped lake basins that formed during deglaciation (Hinderer, 2001). This is consistent
706 with the idea that glaciers receded back into the mountain front during the *ca.* 22-19 ka
707 melting event, especially in the north-eastern Alps (Ivy-Ochs, 2015; Reitner, 2007; van
708 Husen, 2000). By extension, this suggests that the HS 1 melting episode (*ca.* 18-16.5 ka;
709 Toucanne et al., 2015), if it existed at all in the Alps (*e.g.* Ravazzi et al., 2014; Wirsig et al.,
710 2016; Lehmann et al., 2020), impacted only a restricted area and volume of ice. This implies
711 that the forcing that caused the initial retreat of the FIS at *ca.* 22-19 ka was important enough
712 to cause a catastrophic collapse of the AIS. The rapid AIS collapse from *ca.* 22 ka was likely
713 forced by the summer energy of Huybers (2006) that increase from 23.5 ka at 45°N and
714 precede the summer insolation by 1.5 kyr (22 ka at 45°N; Laskar et al., 2004) (Fig. 12e). This
715 suggests that summer energy is a better indicator of glacial variability than insolation intensity

716 (Huybers, 2006), and confirms that the AIS was a highly dynamic ice-sheet (Seguinot et al.,
717 2018).
718 AIS melting events during HS 3 and HS 2 in both the Danube and Po catchments (Fig. 12c)
719 and the substantial FIS recession in the Baltic lowlands (Boswell et al., 2019; Hughes et al.,
720 2016; Toucanne et al., 2015) are concomitant within age-model uncertainties. HS 3 and HS 2
721 in the North Atlantic correspond to cold air and sea-surface temperatures, widespread sea ice
722 and increased iceberg calving and dispersal from surrounding marine-terminating ice margins
723 (Bard et al., 2000; Barker et al., 2009). This is in contrast to the expectation that ice sheets
724 should expand in colder climates and shrink in warmer climates, given constant precipitation.
725 Considering that ablation of land-based ice in mid-latitudes occurs primarily during summer
726 months (Oerlemans et al., 2001), the melting of both the AIS and the FIS during HS 3 and
727 HS 2 (as well as during Greenland Stadial 4 for the AIS) requires a high seasonality in
728 western Europe. High seasonality implies enhanced summertime melting, and thus rising
729 summer temperature, despite severely cool winters and the rapid expansion of sea ice in the
730 North Atlantic as previously discussed by Buizert et al. (2014) and Denton et al. (2005, 2010)
731 for HS 1 and the Younger Dryas cold reversal. High-resolution climate simulations and proxy
732 evidence, including the disintegration of Alps glaciers and the Scottish ice cap, support the
733 occurrence of warm European summers during HS 1 (*i.e.* the so-called Gschnitz stadial in the
734 Alps; Lehmann et al., 2020) and the Younger Dryas (Bromley et al., 2018; Schenk et al.,
735 2018; Magyari et al., 2019). The atmospheric blocking of cold westerly winds over western
736 Europe would be a key mechanism according to Schenk et al. (2018) and such a forcing
737 would have prevailed during HSs of the last glacial period. A strong shift in atmospheric
738 circulation in Europe and over the Alps during and around the LGM (Becker et al., 2016;
739 Beghin et al., 2015; Florineth and Schlüchter, 2000; Ludwig et al., 2016), including
740 millennial-scale climate changes (Luetscher et al., 2015; Monegato et al., 2017), partly
741 support this assumption. Whatever the mechanism responsible for driving stadial decay of the
742 AIS, our results, together with those obtained for the FIS for the last (Toucanne et al., 2015)
743 and penultimate glacial periods (Boswell et al., 2019), strengthens the idea that warm
744 European summers are likely a recurring feature of North Atlantic stadials.
745
746 **8. CONCLUSION**
747
748 The GAS-CS01 and MD04-2790 glacial sedimentary sequences of the Black Sea 'Lake'
749 provide a continuous high-resolution record of the Danube River discharge over the *ca.* 33-

17 ka period. The main results, based on sedimentological, mineralogical and geochemical analysis, are the following:

1. The Danube sediment routing system produced hyperpycnal discharges into the north-west Black Sea throughout the study interval, and their deposits (*i.e.* hyperpycnites) at the GAS-CS01 and MD04-2790 sites provide a continuous, high-resolution paleoflood record of the Danube River at the end of the last glacial period (*ca.* 33-17 ka);

2. Four main periods of enhanced Danube flood frequency (F_x), each of 1.5-3 kyr duration, are recorded at *ca.* 32.5-30.5 ka (F_5), at *ca.* 29-27.5 ka (F_4), at *ca.* 25.3-23.8 ka (F_3) and at *ca.* 22.3-19 ka (F_2). The sediment of the F_2 period are typical of the Alpine foreland, whereas that deposited during the F_5 period shows mineralogical and geochemical signatures typical of the inner Alps (*i.e.* Engadine and Taeurn windows). This suggests that the Danube River activity over the *ca.* 33-17 ka interval provides a valuable record of paleoenvironmental changes in the European Alps, and by extension of the north-eastern AIS, from the second part of MIS 3 to the deglaciation;

3. Our data and continental morphostratigraphical evidence, suggest that the AIS volume has drastically decreased at *ca.* 19 ka (and as soon as *ca.* 22 ka) since no fluctuation of the AIS is recorded at the studied sites after this date. On the other hand, millennial-scale fluctuations of the north-eastern AIS are recorded before the deglacial 22-19 ka event (F_2), with three significant melting episodes, able to remobilize glacigenic sediment to the Black Sea, at *ca.* 32.5-30.5 ka (F_5), at *ca.* 29-27.5 ka (F_4) and at *ca.* 25.3-23.8 ka (F_3). Ice advance occurred between these periods and both the mineralogical and geochemical data suggest that the rapid AIS growth from the inner Alps to its LGM position started from *ca.* 30.5 ka and ended no later than *ca.* 25.3 ka;

4. The F_5 (*ca.* 32.5-30.5 ka), F_4 (*ca.* 29-27.5 ka) and F_3 (*ca.* 25.3-23.8 ka) events indicates enhanced surface melting of the AIS during HS 3 (*ca.* 32-29 ka), Greenland Stadial 4 (*ca.* 28.6-27.8 ka) and HS 2 (*ca.* 26-23.5 ka) when severely cold winters and the rapid expansion of sea ice prevailed in the North Atlantic. This new finding is in line with those recently reported for the southern FIS and reinforces the emerging view that warm summers and hence strong seasonality are key climatic features of western Europe during North Atlantic stadials.

ACKNOWLEDGMENTS

The authors are very grateful to S. Ker, co-chief of the GHASS cruise; T. Dalle-Mulle, J. Gouriou, A. Roubi, M. Rovere and M. Simon for technical support; B. Martin and S. Zaragosi for the preparation of sediment thin sections; A. Trinquier for assistance on the Neptune MC-ICPMS; E. Pelleter for the acquisition of the X-ray EDS maps; N. Gayet for the acquisition of the SEM images; A. Banak, B. Dennielou, T. Gardes, G. Lericolais, A. Mena, R. Silva-Jacinto, A. Van Exem and C. Zavala for invaluable discussions at various stages of this work; A. Chalm for English improvements; and G. Monegato and two anonymous reviewers for their helpful comments, which greatly improved the manuscript. Samples from river banks were collected in one expedition by L.G. and two successive fieldwork seasons by a team from ETH Zurich (the later reported in Freymond et al., 2017). Authors also thank the crew and scientific teams of the ASSEMBLAGE (R/V Marion Dufresne) and GHASS (R/V Pourquoi Pas?) cruises for the recovery of the long-piston cores MD04-2790 and GAS-CS01, respectively. This work is a contribution to the ASSEMBLAGE project funded by the European Commission (EVK3-CT-2002-00090) and to the BLAME project sponsored by the French National Research Agency (ANR-18-CE01-0007). L.G. was supported by internal grants from Woods Hole Oceanographic Institution. Data presented in this study are available in the supplementary material, and through the SEANOE open-source online data repository (https://doi.org/10.17882/70660).

DATA AVAILABILITY

Datasets related to this article can be found at https://doi.org/10.17882/70660, via the SEANOE open-source online data repository.

FIGURE CAPTIONS

Fig. 1: Paleogeography of the Danube sediment routing system at the Last Glacial Maximum (LGM) including the Alpine Ice-Sheet (AIS, ~130,000 km^2; Ehlers and Gibbard, 2004), the river course (~2,900 km; ~801,000 km^2) from the Black Forest (Bf) to the (modern) Danube delta (Dd), and the Danube deep-sea fan (Df; ~20,000 km^2; Danube Canyon and channel-levees in orange) in the Black Sea 'Lake' (level ~90-120 m below the present sea level; paleoshoreline at -120 m in the Black and Adriatic Seas in light blue). A significant part of the Rhine glacier (~14,000 km^2; red arrows) drained into the Danube River at the LGM (Ellwanger et al., 2011), thus increasing the AIS surface in the Danube watershed to ~50,000 km². Filled circles indicate the location of the modern river samples, with the colors referring to the Alpine (white), Dinaric (purple) and Carpathians (green) sources. Orange circles refer to the samples collected along the Danube mainstream (Table 3). Tagl.: Tagliamento glacier; EW: Engadine window; TW: Tauern window (Alps); GW: Gemer-Bürkk window; DW: Danubian window (Carpathians). White stars in the Black Sea indicate the location of cores GAS-CS01 and MD04-2790. Black stars in the north-western Alps and the Adriatic Sea refer to the Sieben Hengste cave system (7H; Luetscher et al., 2015) and the PRAD1-2 borehole (Pellegrini et al., 2017, 2018) respectively. The limits of the Fennoscandian Ice Sheet (FIS) at 22 ka (continuous white line) and 17 ka (dashed white line) are also shown (Hughes et al., 2016). The retreat of the FIS in the upper Dniepr from *ca.* 17 ka caused the deposition of the Red Layers into the Black Sea (Soulet et al., 2013). Note the absence of an ice-sheet on the Carpathians at the LGM.

Fig. 2: Detailed map of the north-western Black Sea margin showing the location of the long-piston cores GAS-CS01 and MD04-2790 in front of the modern Danube delta. The numerous canyons (including the shelf-penetrating Danube Canyon; Popescu et al., 2004) visible on the continental slope are indicative of high Danube sediment discharge and of a good connectivity between the Danube delta and the shelf margin during the last glacial period, when the Black Sea was a giant freshwater lake and lowstand conditions dominated (see Part 2 for details). Danube paleovalleys from Popescu et al. (2004).

Fig. 3: Detailed map of the eastern Alps showing (i) the main geographical and geological features discussed in the main text, including the Tauern (TW) and Engadine (EW) windows (Bousquet et al., 2008); (ii) the main rivers (blue lines) draining into the Danube River (except

844 the Rhine and Adige); (iii) the Alpine Ice-Sheet (AIS) at the LGM (Ehlers and Gibbard,
845 2004). The thick white line shows the AIS ice-divide at the LGM (based on Seguinot et al.,
846 2018). Star labeled 7H: Sieben Hengste cave system (Luetscher et al., 2015).
847
848 **Fig. 4:** Digital photographs and X-ray images of representative sections of the glacial
849 sequence of core GAS-CS01 (*i.e.* 'banded lutites' -Unit III- of Ross and Degens, 1974). Note
850 that the sequence is fully laminated, with clastic rhytmites evolving gradually downward from
851 millimetre- (*i.e.* laminae; Scandinavian-type lacustrine varves of Degens et al., 1978) to
852 decimetre-thick deposits (*i.e.* beds; megavarves of Degens et al., 1978). Clastic rhytmites in
853 GAS-CS01 are interpreted as hyperpycnite sequences. See Figs 7, 8 and 9 for details.
854
855 **Fig. 5:** Stratigraphic correlation between cores GAS-CS01 (magenta line) and MD04-2790
856 (black line; Soulet et al., 2011a) based on XRF-Can_{orm} profiles. See section 5 'Age-depth
857 model' and Supplementary Online Material for details, and Table 2 for the radiocarbon dates.
858
859 **Fig. 6:** Depth-depth relationship between cores GAS-CS01 and MD04-2790 based on the
860 stratigraphic correlations shown in Figure 5. See section 5 'Age-depth model' and
861 Supplementary Online Material for details, and Table 2 for the radiocarbon dates. The
862 laminae / bed thickness and the Red Layers interval are also shown. Note that sediment
863 accumulation rates (SAR) at site GAS-CS01 are significantly higher than at site MD04-2790
864 before *ca.* 31 ka (*i.e.* below depth 1595 cmbsf in core GAS-CS01 and depth 1990 cmbsf in
865 MD04-2790), consistent with the significant thickness difference of hyperpycnal beds
866 observed at the two sites on the same time interval. The decimeter-scale hyperpycnite beds
867 recognized in the lower part of core GAS-CS01 are detailed in Figure 7.
868
869 **Fig. 7:** High-resolution analysis of the pluricentimeter-thick clastic rhytmites, interpreted as
870 hyperpycnites (H), observed in the basal part of core GAS-CS01 (>28.5 mbsf; here Section
871 34/34, 3139-3214 cmbsf; *ca.* 33 ka). **a,** Digital photograph; **b,** X-ray image and grey-level
872 measurements (yellow line); **c,** Hyperspectral image highlighting changes in the sediment
873 texture and/or composition. Colored circles refer to the grain-size analyses shown in **e** and **g**
874 (sedimentary sequences S1, S2 and S3); **d,** Schematic lithological succession based on grain-
875 size (**e**) and XRF (**f**) measurements. H*a* and H*b* correspond to the (basal) coarsening-up (*i.e.*
876 waxing period of river discharge) and (top) fining-up (*i.e.* waning period of discharge)
877 sequences of the hyperpycnites (Mulder et al., 2003) respectively. C: clay. S: silt-sand. **e,**

878 Grain-size measurements (median or D50, *i.e.* grain-size -µm- at which 50% of sample is
879 finer). Mean sampling resolution of 0.25 cm (*n*=218). Black arrows highlight some
880 representative coarsening-up and fining-up sequences. Colored circles refer to the grain-size
881 analyses shown in **c** and **g**; **f,** XRF Zr/Rb ratio, here used as a semi-quantitative grain-size
882 indicator (Dypvik and Harris, 2001); **g,** Particle size distribution of discrete sediment samples
883 (colored circles in **c** and **e**) from the coarsening-up sequences S1, S2 and S3.
884
885 **Fig. 8:** High-resolution analysis of the centimeter-thick clastic rhytmites, interpreted as
886 hyperpycnites (H), observed in the lower part of core GAS-CS01 (from ~22 to 28.5 mbsf;
887 here Section 30/34, 2804-2859 cmbsf; *ca.* 32 ka). **a,** Digital photograph; **b,** X-ray image and
888 grey-level measurements (yellow line); **c,** Hyperspectral image highlighting changes in the
889 sediment texture and/or composition. Colored circles refer to the grain-size analyses shown in
890 **e** and **g** (sedimentary sequences S1, S2, S3 and S4); **d,** Schematic lithological succession
891 based on grain-size (**e**) and XRF (**f**) measurements. H*a* and H*b* correspond to the (basal)
892 coarsening-up (*i.e.* waxing period of river discharge) and (top) fining-up (*i.e.* waning period
893 of discharge) sequences of the hyperpycnites (Mulder et al., 2003) , respectively. C: clay. S:
894 silt-sand; **e,** Grain-size measurements (median or D50, *i.e.* grain-size -µm- at which 50% of
895 sample is finer). Mean sampling resolution of 0.25 cm (*n*=149). Black arrows highlight some
896 representative coarsening-up and fining-up sequences. Colored circles refer to the grain-size
897 analyses shown in **c** and **g**; **f,** XRF Zr/Rb ratio, here used as a semi-quantitative grain-size
898 indicator (Dypvik and Harris, 2001); **g,** Particle size distribution of discrete sediment samples
899 (colored circles in **c** and **e**) from the coarsening-up sequences S1, S2 and S3.
900
901 **Fig. 9:** High-resolution analysis of the subcentimeter-thick clastic rhytmites, interpreted as
902 hyperpycnites (H), observed in core GAS-CS01 (down to ~22 mbsf; here Section 22/34,
903 2031-2083 cmbsf; *ca.* 31 ka). **a,** Digital photograph; **b,** X-ray image and grey-level
904 measurements (yellow line); **c,** Hyperspectral image highlighting changes in the sediment
905 texture and/or composition; **d,** XRF Zr/Rb ratio, here used as a semi-quantitative grain-size
906 indicator (Dypvik and Harris, 2001); **e**, Focus on the XRF Zr/Rb ratio. The Zr/Rb variability,
907 similar to that observed for thicker clastic rhythmites in GAS-CS01 (Figs 7 and 8), suggest
908 coarsening-up and fining-up sequences; **f,** Thin section photograph (2039-2047.5 cmbsf)
909 showing subcentimeter-thick clastic rhytmites. White circles refer to the grain-size analyses
910 shown in **g**. Mean sampling resolution of 0.25 cm (*n*=31); **g,** SEM-EDX image of a
911 coarsening-up sequences (see the red square in **f** for location). The color variability highlights

912 the sediment geochemistry (see the color boxes). Coarse grains are mainly quartz (Si) and
913 dolomite grains (Mg, Ca). Note their angular character. Particle size distribution (white boxes)
914 for clayey (n=9) and silty (n=5) intervals are shown. A schematic lithological succession is
915 proposed on the right. H*a* and H*b* according to Mulder et al. (2003).
916
917 **Fig. 10: a,** $\delta^{18}O$ from GISP2 on the GICC05 timescale and the INTIMATE event stratigraphy.
918 Greenland Stadials (GS) and Greenland Interstadials (GI) are the Greenland expressions of
919 the characteristic Dansgaard-Oeschger events that represent cold and warm phases of the
920 North Atlantic region, respectively (Rasmussen et al., 2014). The Greenland synthetic $\delta^{18}O$
921 record (GLT_syn) of Barker et al. (2011), placed on the absolutely dated Chinese speleothem
922 record (Hulu Cave on this time interval), is also shown; **b, c,** Flood frequency and sediment
923 accumulation rates (SAR) off the Danube River, respectively; **d, e, f,** Clay mineralogy,
924 dolomite abundance and illite crystallinity (three-points average) at core GAS-CS01,
925 respectively. The green arrow highlights the increase in smectite content to higher values,
926 interpreted as the signature of the western Molasse Basin and Rhine glacier in response to the
927 rapid growth of the AIS (see Fig. 11 for details); **g,** Neodymium isotopic composition
928 (expressed in εNd) in core MD04-2790 (*ca.* 28-10 ka; Soulet et al., 2013) and GAS-CS01
929 (*ca.* 33.5-28 ka; this study) as a proxy for sediment provenance. The vertical light blue bars
930 highlight the timing for the F_5 (*ca.* 32.5-30.5 ka), F_4 (*ca.* 29-27.5 ka), F_3 (*ca.* 25.3-23.8 ka), F_2
931 (*ca.* 22.3- 19 ka) and F_1 (*ca.* 17.2-15.7 ka) peaks -based on both the flood frequency (**b**) and
932 the SAR (**c**)- interpreted as periods of enhanced flux of sediment-laden meltwater on the
933 north-west Black Sea margin. HS refers to Heinrich Stadials.
934
935 **Fig. 11:** Paleogeography of the central and eastern Alps, including the hydrographic network
936 (blue lines) and glacial limits (white shaded areas) at (a) *ca.* 33 ka (*i.e.* before Heinrich Stadial
937 3 = F_5 peak at the GAS-CS01 and MD04-2790 sites) and (b) during the local Last Glacial
938 Maximum (LGM; Ehlers and Gibbard, 2004), *ca.* 26 ka (*i.e.* before Heinrich Stadial 2 = F_3
939 peak). The proposed configuration at *ca.* 33 ka is based first on the geochemical evidences
940 (ICr, ε_{Nd}) found at GAS-CS01 for significant inputs of terrigenous material from the Engadine
941 (EW) and Taeurn (TW) windows (purple dashed lines; via the Inn, Salzach, Enns, Mur and
942 Drava rivers) into the north-west Black Sea *ca.* 32.5-30.5 ka (*i.e.* during the F_5 peak
943 interpreted as AIS melting; see the main text for details); and second, on the low content of
944 smectite at the GAS-CS01 site before *ca.* 30.5 ka (and until *ca.* 33.5 ka at least; Fig. 10d). The

945 smectite in the Alpine domain being restricted to the western part of the Molasse Basin (*e.g.*
946 Iller River; Table 3) and the upper Rhine (Müller and Quakernaat, 1969), the clay mineralogy
947 at GAS-CS01 suggests that these areas were mainly free of ice at *ca.* 33 ka (and until
948 *ca.* 30.5 ka) as shown in (a). Such an ice configuration (with the Iller, Lech and Isar/Loisach
949 rivers not connected to the AIS) is found using an equilibrium line altitude at ~2300 m above
950 sea level (white, high-altitude areas; also shown in (b) for comparison). Note that the invasion
951 of the northern Alpine foreland by the major AIS ice-streams (Alpine LGM) strongly
952 modified the glacial hydrographic pattern of the Alpine Danube. Smectite content at GAS-
953 CS01 suggests that the AIS growth (including the Iller glacier; Habbe and Rögner, 1989) and
954 the subsequent re-routing of the Rhine glacier meltwaters to the Danube (Ellwanger et al.,
955 2011) occurred from *ca.* 30.5 ka. The white arrows show the main sources for AIS meltwater
956 to the Danube. HS refers to Heinrich Stadials.
957
958 **Fig. 12: a,** $\delta^{18}O$ from GISP2 (Rasmussen et al., 2014) and the GLT_syn record (Barker et al.,
959 2011). See Fig. 10a for details; **b,** Flood frequency of the Danube River (Fig. 10b). The
960 dashed lines (between *ca.* 17.2 and 15.7 ka) correspond to the Dniepr River flood (Red
961 Layers; Soulet et al., 2013); **c,** Sediment volume of the Po River lowstand wedge, based on
962 seismic reflection data and the PRAD1-2 borehole (Fig. 1; Pellegrini et al., 2017, 2018); **d,**
963 Ice-mass balance of the north-east AIS based on the Danube sediment records (open circles
964 and black line) and the 7H $\delta^{18}O$ record from the Sieben Hengste cave system, Switzerland
965 (Figs 1 and 3; Luetscher et al., 2015). Thick blue arrows highlight AIS melting intervals,
966 meltwater production and sediment-laden meltwater inputs to the north-west Black Sea
967 margin (**b**); **d,** Fluctuations of the Rhine (purple; Preusser et al., 2011) and Tagliamento
968 (green; Monegato et al., 2007) glaciers. Arrows highlight the glaciers fluctuations discussed in
969 the main text; **e,** Summer energy (red line, τ ~ 400) (Huybers, 2006) and 21 June-20 July
970 insolation for 45°N (blue line; Laskar et al., 2004). The vertical light blue bars highlight the
971 timing for the F_5 (*ca.* 32.5-30.5 ka), F_4 (*ca.* 29-27.5 ka), F_3 (*ca.* 25.3-23.8 ka), F_2 (*ca.* 22.3-
972 19 ka) and F_1 (*ca.* 17.2-15.7 ka) flood events. HS refers to Heinrich Stadials.

973 **TABLE CAPTIONS**

974

975 **Table 1:** Core locations.

976

977 **Table 2:** New radiocarbon (^{14}C) dates for cores GAS-CS01 and MD04-2790. Analyses were
978 carried out at the Beta Analytic radiocarbon dating laboratory (USA).

979

980 **Table 3:** Clay mineralogy of the Danube River and its main tributaries. Geographic
981 'mountainous' clusters (raw -†- and weighted -‡- mean values considering the river drainage
982 surface, with the upper Drava excluded in the latter calculation) correspond to the main
983 sediment sources of the Danube watershed. Note that the weighted mean clay mineralogy of
984 these clusters (*i.e.* Alps + Dinarides + Carpathians) is close to that obtained for the Danube
985 River mainstream.

REFERENCES

Aksu, A.E., Hiscott, R.N., Kaminski, M.A., Mudie, P.J., Gillespie, H., Abrajano, T., Yaşar, D., 2002. Last glacial–Holocene paleoceanography of the Black Sea and Marmara Sea: stable isotopic, foraminiferal and coccolith evidence. Mar. Geol. 190, 119–149. https://doi.org/10.1016/S0025-3227(02)00345-6

Árkai, P., 1991. Chlorite crystallinity: an empirical approach and correlation with illite crystallinity, coal rank and mineral facies as exemplified by Palaeozoic and Mesozoic rocks of northeast Hungary. Journal of metamorphic Geology 9, 723–734. https://doi.org/10.1111/j.1525-1314.1991.tb00561.x

Árkai, P., Faryad, S.W., Vidal, O., Balogh, K., 2003. Very low-grade metamorphism of sedimentary rocks of the Meliata unit, Western Carpathians, Slovakia: implications of phyllosilicate characteristics. International Journal of Earth Sciences 92, 68–85. https://doi.org/10.1007/s00531-002-0303-x

Asch, K., Bellenberg, S., Comission for geological Map of the World, 2005. The 1: 5 million international geological map of Europe and adjacent areas (IGME 5000). Bundesanstalt für Geowissenschaften und Rohstoffe.

Badertscher, S., Fleitmann, D., Cheng, H., Edwards, R.L., Göktürk, O.M., Zumbühl, A., Leuenberger, M., Tüysüz, O., 2011. Pleistocene water intrusions from the Mediterranean and Caspian seas into the Black Sea. Nat. Geosci. 4 (4), 236-239. https://doi.org/10.1038/NGEO1106

Bahr, A., Arz, H.W., Lamy, F., Wefer, G., 2006. Late glacial to Holocene paleoenvironmental evolution of the Black Sea, reconstructed with stable oxygen isotope records obtained on ostracod shells. Earth Planet. Sci. Lett. 241 (3-4), 863-875. https://doi.org/10.1016/j.epsl.2005.10.036

Bahr, A., Lamy, F., Arz, H., Kuhlmann, H., Wefer, G., 2005. Late glacial to Holocene climate and sedimentation history in the NW Black Sea. Mar. Geol. 214 (4), 309-322. https://doi.org/10.1016/j.margeo.2004.11.013

Bahr, A., Lamy, F., Arz, H.W., Major, C., Kwiecien, O., Wefer, G., 2008. Abrupt changes of temperature and water chemistry in the late Pleistocene and early Holocene Black Sea. Geochem. Geophys. Geosyst. 9. https://doi.org/10.1029/2007GC001683

Bard, E., Rostek, F., Turon, J.-L., Gendreau, S., 2000. Hydrological impact of Heinrich events in the subtropical northeast Atlantic. Science 289, 1321–1324. https://doi.org/10.1126/science.289.5483.1321

Bard, E., Rostek, F., Ménot-Combes, G., 2004. Radiocarbon calibration beyond 20,000 ^{14}C yr BP by means of planktonic foraminifera of the Iberian Margin. Quat. Res. 61(2), 204-214. https://doi.org/10.1016/j.yqres.2003.11.006

Bard, E., Ménot, G., Rostek, F., Licari, L., Böning, P., Edwards, R. L., Cheng, H., Wang, Y., Heaton, T. J., 2013. Radiocarbon calibration/comparison records based on marine sediments from the Pakistan and Iberian margins. Radiocarbon, 55(4), 1999-2019. https://doi.org/10.2458/azu_js_rc.55.17114

Barker, S., Diz, P., Vautravers, M.J., Pike, J., Knorr, G., Hall, I.R., Broecker, W.S., 2009. Interhemispheric Atlantic seesaw response during the last deglaciation. Nature 457 (7233), 1097. https://doi.org/10.1038/nature07770

Barker, S., Knorr, G., Edwards, R. L., Parrenin, F., Putnam, A. E., Skinner, L. C., Wolff, E., Ziegler, M., 2011. 800,000 years of abrupt climate variability. Science, 334 (6054), 347-351. https://doi.org/10.1126/science.1203580

Bayon, G., Barrat, J.A., Etoubleau, J., Benoit, M., Bollinger, C., Révillon, S., 2009. Determination of rare earth elements, Sc, Y, Zr, Ba, Hf and Th in geological samples by ICP-MS after Tm addition and alkaline fusion. Geostandards and Geoanalytical Research 33, 51–62. https://doi.org/10.1111/j.1751-908X.2008.00880.x

Bayon, G., German, C.R., Boella, R.M., Milton, J.A., Taylor, R.N., Nesbitt, R.W., 2002. An improved method for extracting marine sediment fractions and its application to Sr and Nd isotopic analysis. Chem. Geol. 187, 179–199. https://doi.org/10.1016/S0009-2541(01)00416-8

Bayon, G., Toucanne, S., Skonieczny, C., André, L., Bermell, S., Cheron, S., Dennielou, B., Etoubleau, J., Freslon, N., Gauchery, T., Germain, Y., Jorry, S.J., Ménot, G., Monin, L., Ponzevera, E., Rouget, M.-L., Tachikawa, K., Barrat, J.A., 2015. Rare earth elements and neodymium isotopes in world river sediments revisited. Geochimica et Cosmochimica Acta 170, 17–38. https://doi.org/10.1016/j.gca.2015.08.001

Becker, P., Seguinot, J., Jouvet, G., Funk, M., 2016. Last Glacial Maximum precipitation pattern in the Alps inferred from glacier modelling. Geographica Helvetica 71, 173–187. https://doi.org/10.5194/gh-71-173-2016

Beghin, P., Charbit, S., Dumas, C., Kageyama, M., Ritz, C., 2015. How might the North American ice sheet influence the northwestern Eurasian climate? Clim. Past Discussions 11, 1467–1490. https://doi.org/10.5194/cp-11-1467-2015

Blöschl, G., Nester, T., Komma, J., Parajka, J., Perdigão, R.A., 2013. The June 2013 flood in the Upper Danube Basin, and comparisons with the 2002, 1954 and 1899 floods. Hydrology and Earth System Sciences 17, 5197–5212. https://doi.org/10.5194/hess-17-5197-2013

Blum, M.D., Törnqvist, T.E., 2000. Fluvial responses to climate and sea-level change: a review and look forward. Sedimentology 47, 2–48. https://doi.org/10.1046/j.1365-3091.2000.00008.x

Bobos, I., 2012. Characterization of smectite to NH4-illite conversion series in the fossil hydrothermal system of Harghita Bãi, East Carpathians, Romania. American Mineralogist 97, 962–982. https://doi.org/10.2138/am.2012.3801

Bonneau, L., Jorry, S.J., Toucanne, S., Silva Jacinto, R., Emmanuel, L., 2014. Millennial-scale response of a western Mediterranean river to late Quaternary climate changes: a view from the deep sea. J. Geol. 122, 687–703. https://doi.org/10.1086/677844

Bonneau, L., Toucanne, S., Bayon, G., Jorry, S.J., Emmanuel, L., Jacinto, R.S., 2017. Glacial erosion dynamics in a small mountainous watershed (Southern French Alps): A source-to-sink approach. Earth Planet. Sci. Lett. 458, 366–379. https://doi.org/10.1016/j.epsl.2016.11.004

Boswell, S.M., Toucanne, S., Creyts, T.T., Hemming, S.R., 2018. Continental-scale transport of sediments by the Baltic Ice Stream elucidated by coupled grain size and Nd provenance analyses. Earth Planet. Sci. Lett. 490, 143–150. https://doi.org/10.1016/j.epsl.2018.03.017

Boswell, S.M., Toucanne, S., Pitel-Roudaut, M., Creyts, T.T., Eynaud, F., Bayon, G., 2019. Enhanced surface melting of the Fennoscandian Ice Sheet during periods of North Atlantic cooling. Geology 47 (7), 664-668. https://doi.org/10.1130/G46370.1

Bousquet, R., Oberhänsli, R., Goffé, B., Wiederkehr, M., Koller, F., Schmid, S.M., Schuster, R., Engi, M., Berger, A., Martinotti, G., 2008. Metamorphism of metasediments at the scale of an orogen: a key to the Tertiary geodynamic evolution of the Alps. Geological Society, London, Special Publications 298, 393–411. https://doi.org/10.1144/SP298.18

Bromley, G., Putnam, A., Borns, H., Lowell, T., Sandford, T., Barrell, D., 2018. Interstadial Rise and Younger Dryas Demise of Scotland's Last Ice Fields. Paleoceanography and Paleoclimatology 33, 412–429. https://doi.org/10.1002/2018PA003341

Bronk Ramsey, C., 2001. Development of the Radiocarbon Calibration Program. Radiocarbon 43, 355–363. https://doi.org/10.1017/S0033822200038212

Bronk Ramsey, C., 2008. Deposition models for chronological records. Quat. Sci. Rev., 27 (1-2), 42-60. https://doi.org/10.1016/j.quascirev.2007.01.019

Bronk Ramsey, C., 2009. Bayesian analysis of radiocarbon dates. Radiocarbon, 51 (1), 337-360. https://doi.org/10.1017/S0033822200033865

Bronk Ramsey, C., 2017. Methods for summarizing radiocarbon datasets. Radiocarbon, 59 (6), 1809-1833. https://doi.org/10.1017/RDC.2017.108

Bronk Ramsey, C., Lee, S., 2013. Recent and Planned Developments of the Program OxCal. Radiocarbon 55, 720–730. https://doi.org/10.1017/S0033822200057878

Brown, P.A., Kennett, J.P., 1998. Megaflood erosion and meltwater plumbing changes during last North American deglaciation recorded in Gulf of Mexico sediments. Geology 26, 599–602. https://doi.org/10.1130/0091-7613(1998)026<0599:MEAMPC>2.3.CO;2

Busschers, F.S., Kasse, C., Van Balen, R.T., Vandenberghe, J., Cohen, K.M., Weerts, H.J.T., Wallinga, J., Johns, C., Cleveringa, P., Bunnik, F.P.M., 2007. Late Pleistocene evolution of the Rhine-Meuse system in the southern North Sea basin: imprints of climate change, sea-level oscillation and glacio-isostacy. Quat. Sci. Rev. 26, 3216–3248. https://doi.org/10.1016/j.quascirev.2007.07.013

Carlson, A.E., Clark, P.U., 2012. Ice sheet sources of sea level rise and freshwater discharge during the last deglaciation. Rev. Geophys. 50. http://doi.org/10.1029/2011RG000371

Chaline, J., Jerz, H., 1984. Arbeitsergebnisse der Subkommission für Europäische Quartärstratigraphie. Stratotypen des Würm-Glazials. Eiszeitalter und Gegenwart 35, 185–206.

Chamley, H., 1989. Clay sedimentology, Springer-Verlag. ed. New York.

Ciulavu, M., Mählmann, R.F., Schmid, S.M., Hofmann, H., Seghedi, A., Frey, M., 2008. Metamorphic evolution of a very low-to low-grade metamorphic core complex (Danubian window) in the South Carpathians. Geological Society, London, Special Publications 298, 281–315. https://doi.org/10.1144/SP298.14

Clark, P.U., Dyke, A.S., Shakun, J.D., Carlson, A.E., Clark, J., Wohlfarth, B., Mitrovica, J.X., Hostetler, S.W., McCabe, A.M., 2009. The last glacial maximum. Science 325, 710–714. https://doi.org/10.1126/science.1172873

Comiti, F., Mao, L., Penna, D., Dell'Agnese, A., Engel, M., Rathburn, S., Cavalli, M., 2019. Glacier melt runoff controls bedload transport in Alpine catchments. Earth and Planet.Sci. Lett.520, 77-86. https://doi.org/10.1016/j.epsl.2019.05.031

Constantinescu, A.M., Toucanne, S., Dennielou, B., Jorry, S.J., Mulder, T., Lericolais, G., 2015. Evolution of the Danube Deep-Sea Fan since the Last Glacial Maximum: new insights into Black Sea water-level fluctuations. Mar. Geol. 367, 50–68. https://doi.org/10.1016/j.margeo.2015.05.007

Coulthard, T.J., Lewin, J., Macklin, M.G., 2005. Modelling differential catchment response to environmental change. Geomorphology 69, 222–241. https://doi.org/10.1016/j.geomorph.2005.01.008

Covault, J.A., Romans, B.W., Graham, S.A., Fildani, A., Hilley, G.E., 2011. Terrestrial source to deep-sea sink sediment budgets at high and low sea levels: Insights from tectonically active Southern California. Geology 39, 619–622. https://doi.org/10.1130/G31801.1

de Leeuw, A., Morton, A., van Baak, C.G.C., Vincent, S.J., 2018. Timing of arrival of the Danube to the Black Sea: Provenance of sediments from DSDP site 380/380A. Terra Nova 30, 114–124. https://doi.org/10.1111/ter.12314

Dean, W.E., Arthur, M.A., 2011. Geochemical characteristics of Holocene laminated sapropel (unit II) and underlying lacustrine unit III in the Black Sea (Report n°. 2010–1323), Open-File Report. https://doi.org/10.3133/ofr20101323

Debret, M., Copard, Y., Van Exem, A., Bessereau, G., Haeseler, F., Rouzaud, J.N., 2018. The color of refractory organic carbon. Bulletin de la Société Géologique de France 189 (2), 9. https://doi.org/10.1051/bsgf/2018008

Degens, E.T., Ross, D.A., 1972. Chronology of the Black Sea over the last 25,000 years. Chem. Geol. 10, 1–16. https://doi.org/10.1016/0009-2541(72)90073-3

Degens, E.T., Stoffers, P., Golubic, S., 1978. Varve chronology: Estimated rates of sedimentation in the Black Sea Basin. In D. A. Ross (Ed.), Initial report of the deep sea drilling project (Vol. 42, Part 2, pp. 499–508). Washington, D.C.: U.S. Government Printing Office.

Deuser, W.G., 1972. Late Pleistocene and Holocene history of the Black Sea as indicated by stable isotope studies. J. Geophys. Res. 77, 1071–1077.

Dypvik, H., Harris, N.B., 2001. Geochemical facies analysis of fine-grained siliciclastics using Th/U, Zr/Rb and (Zr+Rb)/Sr ratios. Chem. Geol. 181, 131-146. https://doi.org/10.1016/S0009-2541(01)00278-9

Eglinton, T.I., Benitez-Nelson, B.C., Pearson, A., McNichol, A.P., Bauer, J.E., Druffel, E.R., 1997. Variability in radiocarbon ages of individual organic compounds from marine sediments. Science 277, 796–799. https://doi.org/10.1126/science.277.5327.796

Ehlers, J., Gibbard, P.L., 2004. Quaternary glaciations-extent and chronology: part I: Europe. Elsevier.

Ellwanger, D., Wielandt-Schuster, U., Franz, M., Simon, T., 2011. The Quaternary of the southwest German Alpine Foreland (Bodensee-Oberschwaben, Baden-Württemberg, Southwest Germany). Quat. Sci. J. 60, 306–328. https://doi.org/10.3285/eg.60.2-3.07

Fitzsimmons, K.E., Marković, S.B., Hambach, U., 2012. Pleistocene environmental dynamics recorded in the loess of the middle and lower Danube basin. Quat. Sci. Rev. 41, 104–118. https://doi.org/10.1016/j.quascirev.2012.03.002

Florineth, D., Schlüchter, C., 2000. Alpine evidence for atmospheric circulation patterns in Europe during the Last Glacial Maximum. Quat. Res. 54, 295–308. https://doi.org/10.1006/qres.2000.2169

Freymond, C.V., Peterse, F., Fischer, L.V., Filip, F., Giosan, L., Eglinton, T.I., 2017. Branched GDGT signals in fluvial sediments of the Danube River basin: Method comparison and longitudinal evolution. Org. Geochem. 103, 88–96. https://doi.org/10.1016/j.orggeochem.2016.11.002

Frost, C.D., O'Nions, R.K., Goldstein, S.L., 1986. Mass balance for Nd in the Mediterranean Sea. Chem. Geol. 55, 45–50. https://doi.org/10.1016/0009-2541(86)90126-9

Gábris, G., Nádor, A., 2007. Long-term fluvial archives in Hungary: response of the Danube and Tisza rivers to tectonic movements and climatic changes during the Quaternary: a review and new synthesis. Quat. Sci. Rev. 26, 2758–2782. https://doi.org/10.1016/j.quascirev.2007.06.030

Garnier, J., Billen, G., Hannon, E., Fonbonne, S., Videnina, Y., Soulie, M., 2002. Modelling the Transfer and Retention of Nutrients in the Drainage Network of the Danube River. Estuarine, Coastal and Shelf Science 54, 285–308. https://doi.org/10.1006/ecss.2000.0648

Gibbard, P.L., 1988. The history of the great northwest European rivers during the past three million years. Philosophical Transactions of the Royal Society of London. B, Biol. Sci. 318, 559–602. https://doi.org/10.1098/rstb.1988.0024

Giosan, L., Donnelly, J.P., Constantinescu, S., Filip, F., Ovejanu, I., Vespremeanu-Stroe, A., Vespremeanu, E., Duller, G.A., 2006. Young Danube delta documents stable Black Sea level since the middle Holocene: Morphodynamic, paleogeographic, and archaeological implications. Geology 34, 757–760. https://doi.org/10.1130/G22587.1

Giosan, L., Donnelly, J.P., Vespremeanu, E., Bhattacharya, J.P., Olariu, C., Buonaiuto, F.S., 2005. River delta morphodynamics: Examples from the Danube delta. L. Giosan, J.P. Bhattacharya (Eds.), River Deltas - Concepts, Models and Examples, SEPM Special Publication, 83 (2005), pp. 393-411.

Glur, L., Wirth, S.B., Büntgen, U., Gilli, A., Haug, G.H., Schär, C., Beer, J., Anselmetti, F.S., 2013. Frequent floods in the European Alps coincide with cooler periods of the past 2500 years. Sci. Rep. 3, 2770. https://doi.org/10.1038/srep02770

Goldstein, S.J., Jacobsen, S.B., 1988. Nd and Sr isotopic systematics of river water suspended material: implications for crustal evolution. Earth Planet. Sci. Lett. 87, 249–265. https://doi.org/10.1016/0012-821X(88)90013-1

Goodbred Jr, S.L., Kuehl, S.A., 2000. Enormous Ganges-Brahmaputra sediment discharge during strengthened early Holocene monsoon. Geology 28, 1083–1086. https://doi.org/10.1130/0091-7613(2000)28<1083:EGSDDS>2.0.CO;2

Gorlach, A., Hang, T., Kalm, V., 2017. GIS-based reconstruction of Late Weichselian proglacial lakes in northwestern Russia and Belarus. Boreas 46, 486–502. https://doi.org/10.1111/bor.12223

Grosswald, M.G., 1980. Late Weichselian ice sheet of northern Eurasia. Quaternary Research 13, 1–32. https://doi.org/10.1016/0033-5894(80)90080-0

Guichard, F., Carey, S., Arthur, M.A., Sigurdsson, H., Arnold, M., 1993. Tephra from the Minoan eruption of Santorini in sediments of the Black Sea. Nature 363, 610. https://doi.org/10.1038/363610a0

Habbe, K.A., Rögner, K., 1989. The Pleistocene Iller Glaciers and their outwash fields. Catena Supplement 15, 311–328.

Haeberli, W., 1983. Frequency and characteristics of glacier floods in the Swiss Alps. Annals of Glaciology 4, 85–90. https://doi.org/10.3189/S026030550000528

Hallet, B., Hunter, L., Bogen, J., 1996. Rates of erosion and sediment evacuation by glaciers: A review of field data and their implications. Glob. Planet. Chang.12, 213–235. https://doi.org/10.1016/0921-8181(95)00021-6

Heaton, T. J., Bard, E., & Hughen, K. A., 2013. Elastic tie-pointing-transferring chronologies between records via a Gaussian process. Radiocarbon, 55(4), 1975-1997. https://doi.org/10.2458/azu_js_rc.55.17777

Heiri, O., Koinig, K.A., Spötl, C., Barrett, S., Brauer, A., Drescher-Schneider, R., Gaar, D., Ivy-Ochs, S., Kerschner, H., Luetscher, M., 2014. Palaeoclimate records 60–8 ka in the Austrian and Swiss Alps and their forelands. Quat. Sci. Rev. 106, 186–205. https://doi.org/10.1016/j.quascirev.2014.05.021

Hemming, S.R., 2004. Heinrich events: Massive late Pleistocene detritus layers of the North Atlantic and their global climate imprint. Rev. Geophys. 42. https://doi.org/10.1029/2003RG000128

Henry, F., Jeandel, C., Dupre, B., Minster, J.-F., 1994. Particulate and dissolved Nd in the western Mediterranean Sea: sources, fate and budget. Mar. Chem. 45, 283–305. https://doi.org/10.1016/0304-4203(94)90075-2

Hinderer, M., 2001. Late Quaternary denudation of the Alps, valley and lake fillings and modern river loads. Geodinamica Acta 14, 231–263. https://doi.org/10.1080/09853111.2001.11432446

Hinderer, M., Kastowski, M., Kamelger, A., Bartolini, C., Schlunegger, F., 2013. River loads and modern denudation of the Alps: a review. Earth. Sci. Rev. 118, 11–44. https://doi.org/10.1016/j.earscirev.2013.01.001

Hughes, A.L.C., Gyllencreutz, R., Lohne, Ø.S., Mangerud, J., Svendsen, J.I., 2016. The last Eurasian ice sheets - a chronological database and time-slice reconstruction, DATED-1. Boreas 45, 1–45. https://doi.org/10.1111/bor.12142

Hughes, P.D., Woodward, J.C., Van Calsteren, P.C., Thomas, L.E., 2011. The glacial history of the Dinaric Alps, Montenegro. Quat. Sci.Rev. 30, 3393–3412. https://doi.org/10.1016/j.quascirev.2011.08.016

Huybers, P., 2006. Early Pleistocene glacial cycles and the integrated summer insolation forcing. Science 313, 508–511. https://doi.org/10.1126/science.1125249

Ivy-Ochs, S., 2015. Glacier variations in the European Alps at the end of the last glaciation. Cuadernos de Investigación Geográfica 41, 295. https://doi.org/10.18172/cig.2750

Ivy-Ochs, S., Kerschner, H., Reuther, A., Preusser, F., Heine, K., Maisch, M., Kubik, P.W., Schlüchter, C., 2008. Chronology of the last glacial cycle in the European Alps. J. Quat. Sci. 23, 559–573. https://doi.org/10.1002/jqs.1202

Ivy-Ochs, S., Lucchesi, S., Baggio, P., Fioraso, G., Gianotti, F., Monegato, G., Graf, A.A., Akçar, N., Christl, M., Carraro, F., Forno, M.G., Schlüchter, C., 2018. New geomorphological and chronological constraints for glacial deposits in the Rivoli-Avigliana end-moraine system and the lower Susa Valley (Western Alps, NW Italy). J. Quat. Sci. 33, 550–562. https://doi.org/10.1002/jqs.3034

Ivy-Ochs, S., Schäfer, J., Kubik, P.W., Synal, H.-A., Schlüchter, C., 2004. Timing of deglaciation on the northern Alpine foreland (Switzerland). Eclogae Geologicae Helvetiae 97, 47–55.

Jacobsen, S.B., Wasserburg, G.J., 1980. Sm-Nd isotopic evolution of chondrites. Earth Planet. Sci. Lett. 50, 139–155. https://doi.org/10.1016/0012-821X(80)90125-9

Jacq, K., Perrette, Y., Fanget, B., Sabatier, P., Coquin, D., Martinez-Lamas, R., Debret, M., Arnaud, F., 2019. High-resolution prediction of organic matter concentration with hyperspectral imaging on a sediment core. Science of the Total Environment 663, 236–244. https://doi.org/10.1016/j.scitotenv.2019.01.320

Jaeger, J.M., Koppes, M.N., 2016. The role of the cryosphere in source-to-sink systems. Earth Sci. Rev. 153, 43–76. https://doi.org/10.1016/j.earscirev.2015.09.011

Jiao, R., Herman, F., Beyssac, O., Adatte, T., Cox, S.C., Nelson, F.E., Neil, H.L., 2018. Erosion of the Southern Alps of New Zealand during the last deglaciation. Geology 46, 975–978. https://doi.org/10.1130/G45160.1

Jones, G.A., Gagnon, A.R., 1994. Radiocarbon chronology of Black Sea sediments. Deep-Sea Res. Part I: Oceanogr. 41, 531–557. https://doi.org/10.1016/0967-0637(94)90094-9

Juteau, M., Michard, A., Albarede, F., 1986. The Pb-Sr-Nd isotope geochemistry of some recent circum-Mediterranean granites. Contributions to Mineralogy and Petrology 92, 331–340.

Karabanov, A.K., Matveyev, A.V., 2011. The Pleistocene glaciations in Belarus. Quaternary Sciences. Elsevier, pp. 29–35. https://doi.org/10.1016/B978-0-444-53447-7.00003-9

Kasse, C., Bohncke, S.J.P., Vandenberghe, J., Gábris, G., 2010. Fluvial style changes during the last glacial–interglacial transition in the middle Tisza valley (Hungary). Proceedings of the Geologists' Association 121, 180–194. https://doi.org/10.1016/j.pgeola.2010.02.005

Ker, S., Riboulot, V., 2015. GHASS cruise, R/V Pourquoi Pas?. https://doi.org/10.17600/15000500

Kisch, H.J., 1991. Illite crystallinity: recommendations on sample preparation, X-ray diffraction settings, and interlaboratory samples. Journal of Metamorphic Geology 9, 665–670. https://doi.org/10.1111/j.1525-1314.1991.tb00556.x

Kiss, P., Gméling, K., Molnár, F., Pécskay, Z., 2010. Geochemistry of Sarmatian volcanic rocks in the Tokaj Mts (NE Hungary) and their relationship to hydrothermal mineralization. Central European Geology 53, 377–403. https://doi.org/10.1556/CEuGeol.53.2010.4.3

Kolla, V., Perlmutter, M.A., 1993. Timing of turbidite sedimentation on the Mississippi Fan. Aapg Bulletin 77, 1129–1141.

Krinsley, D.H., Donahue, J., 1968. Environmental interpretation of sand grain surface textures by electron microscopy. GSA Bulletin 79, 743–748. https://doi.org/10.1130/0016-7606(1968)79[743:EIOSGS]2.0.CO;2

Krumm, H., Petschick, R., Wolf, M., 1988. From diagenesis to anchimetamorphism, upper Austroalpine sedimentary cover in Bavaria and Tyrol. Geodinamica Acta 2, 33–47. https://doi.org/10.1080/09853111.1988.11105154

Kubler, B., 1967. La cristallinité de l'illite et les zones tout à fait supérieures du métamorphisme. Etages tectoniques 105–121.

Kusch, S., Rethemeyer, J., Schefuß, E., Mollenhauer, G., 2010. Controls on the age of vascular plant biomarkers in Black Sea sediments. Geochimica et Cosmochimica Acta 74, 7031–7047. https://doi.org/10.1016/j.gca.2010.09.005

Kwiecien, O., Arz, H.W., Lamy, F., Wulf, S., Bahr, A., Röhl, U., Haug, G.H., 2008. Estimated reservoir ages of the black sea since the last glacial. Radiocarbon 50, 99–118. https://doi.org/10.1017/S0033822200043393

Larsen, N.K., Knudsen, K.L., Krohn, C.F., Kronborg, C., Murray, A.S., Nielsen, O.B., 2009. Late Quaternary ice sheet, lake and sea history of southwest Scandinavia–a synthesis. Boreas 38, 732–761. https://doi.org/10.1111/j.1502-3885.2009.00101.x

Laskar, J., Robutel, P., Joutel, F., Gastineau, M., Correia, A.C.M., Levrard, B., 2004. A long-term numerical solution for the insolation quantities of the Earth. Astronomy & Astrophysics 428, 261–285. https://doi.org/10.1051/0004-6361:20041335

Lehmann, B., Herman, F., Valla, P.G., King, G.E., Biswas, R.H., Ivy-Ochs, S., Steinemann, O., Christl, M., 2020. Postglacial erosion of bedrock surfaces and deglaciation timing: New insights from the Mont Blanc massif (western Alps). Geology 48. https://doi.org/10.1130/G46585.1

Lericolais, G., 2004. ASSEMBLAGE-1 cruise, R/V Marion Dufresne. https://doi.org/10.17600/4200070

Lericolais, G., Bourget, J., Popescu, I., Jermannaud, P., Mulder, T., Jorry, S., Panin, N., 2013. Late Quaternary deep-sea sedimentation in the western Black Sea: New insights from recent coring and seismic data in the deep basin. Glob. Planet. Chang. 103, 232–247. https://doi.org/10.1016/j.gloplacha.2012.05.002

Lericolais, G., Guichard, F., Morigi, C., Popescu, I., Bulois, C., Gillet, H., Ryan, W.B.F., 2011. Assessment of Black Sea water-level fluctuations since the Last Glacial Maximum. Geology and Geoarchaeology of the Black Sea Region: Beyond the Flood Hypothesis 473, 33.

Ludwig, P., Schaffernicht, E.J., Shao, Y., Pinto, J.G., 2016. Regional atmospheric circulation over Europe during the Last Glacial Maximum and its links to precipitation. Journal of Geophysical Research: Atmospheres 121, 2130–2145. https://doi.org/10.1002/2015JD024444

Luetscher, M., Boch, R., Sodemann, H., Spötl, C., Cheng, H., Edwards, R.L., Frisia, S., Hof, F., Müller, W., 2015. North Atlantic storm track changes during the Last Glacial Maximum recorded by Alpine speleothems. Nature Com. 6. https://doi.org/10.1038/ncomms7344

Macklin, M.G., Benito, G., Gregory, K.J., Johnstone, E., Lewin, J., Michczyńska, D.J., Soja, R., Starkel, L., Thorndycraft, V.R., 2006. Past hydrological events reflected in the Holocene fluvial record of Europe. Catena 66, 145–154. https://doi.org/10.1016/j.catena.2005.07.015

Macklin, M.G., Johnstone, E., Lewin, J., 2005. Pervasive and long-term forcing of Holocene river instability and flooding in Great Britain by centennial-scale climate change. The Holocene 15, 937–943. https://doi.org/10.1191/0959683605hl867ft

Macklin, M.G., Lewin, J., 2003. River sediments, great floods and centennial-scale Holocene climate change. J. Quat. Sci. 18, 101–105. https://doi.org/10.1002/jqs.751

Macklin, M.G., Lewin, J., Woodward, J.C., 2012. The fluvial record of climate change. Philosophical Transactions of the Royal Society A: Mathematical, Physical and Engineering Sciences 370, 2143–2172. https://doi.org/10.1098/rsta.2011.0608

Magyari, E. K., Pál, I., Vincze, I., Veres, D., Jakab, G., Braun, M., Szalai, Z., Szabo, Z., Korponai, J., 2019. Warm Younger Dryas summers and early late glacial spread of temperate deciduous trees in the Pannonian Basin during the last glacial termination (20-9 kyr cal BP). Quat. Sci. Rev., 225, 105980. https://doi.org/10.1016/j.quascirev.2019.105980

Major, C., Ryan, W., Lericolais, G., Hajdas, I., 2002. Constraints on Black Sea outflow to the Sea of Marmara during the last glacial–interglacial transition. Mar. Geol. 190 (1-2), 19-34. https://doi.org/10.1016/S0025-3227(02)00340-7

Major, C.O., Goldstein, S.L., Ryan, W.B., Lericolais, G., Piotrowski, A.M., Hajdas, I., 2006. The co-evolution of Black Sea level and composition through the last deglaciation and its paleoclimatic significance. Quat. Sic. Rev. 25, 2031–2047. https://doi.org/10.1016/j.quascirev.2006.01.032

Makos, M., Dzierżek, J., Nitychoruk, J., Zreda, M., 2014. Timing of glacier advances and climate in the High Tatra Mountains (Western Carpathians) during the Last Glacial Maximum. Quat. Res. 82, 1–13. https://doi.org/10.1016/j.yqres.2014.04.001

Makos, M., Nitychoruk, J., Zreda, M., 2013. Deglaciation chronology and paleoclimate of the Pięciu Stawów Polskich/Roztoki Valley, high Tatra Mountains, Western Carpathians, since the Last Glacial Maximum, inferred from 36Cl exposure dating and glacier–climate modelling. Quat. Int. 293, 63–78. https://doi.org/10.1016/j.quaint.2012.01.016

Makos, M., Rinterknecht, V., Braucher, R., Tołoczko-Pasek, A., Arnold, M., Aumaître, G., Bourlès, D., Keddadouche, K., 2018. Last Glacial Maximum and Lateglacial in the Polish High Tatra Mountains - Revised deglaciation chronology based on the 10 Be exposure age dating. Quat. Sci. Rev. 187, 130–156. https://doi.org/10.1016/j.quascirev.2018.03.006

Makshaev, R.R., Svitoch, A.A., 2016. Chocolate clays of the Northern Caspian Sea Region: Distribution, structure, and origin. Quat. Int. 409, 44–49. https://doi.org/10.1016/j.quaint.2015.07.018

Mangerud, J., Jakobsson, M., Alexanderson, H., Astakhov, V., Clarke, G.K., Henriksen, M., Hjort, C., Krinner, G., Lunkka, J.-P., Möller, P., 2004. Ice-dammed lakes and rerouting of the drainage of northern Eurasia during the Last Glaciation. Quat. Sic. Rev. 23, 1313–1332. https://doi.org/10.1016/j.quascirev.2003.12.009

Marković, S.B., Stevens, T., Kukla, G.J., Hambach, U., Fitzsimmons, K.E., Gibbard, P., Buggle, B., Zech, M., Guo, Z., Hao, Q., Wu, H., O'Hara Dhand, K., Smalley, I.J., Újvári, G., Sümegi, P., Timar-Gabor, A., Veres, D., Sirocko, F., Vasiljević, D.A., Jary, Z., Svensson, A., Jović, V., Lehmkuhl, F., Kovács, J., Svirčev, Z., 2015. Danube loess stratigraphy - Towards a pan-European loess stratigraphic model. Earth Sci. Rev. 148, 228–258. https://doi.org/10.1016/j.earscirev.2015.06.005

Marret, F., Mudie, P., Aksu, A., Hiscott, R. N., 2009. A Holocene dinocyst record of a two-step transformation of the Neoeuxinian brackish water lake into the Black Sea. Quat. Int. 197(1-2), 72-86. https://doi.org/10.1016/j.quaint.2007.01.010

Matenco, L., Andriessen, P., 2013. Quantifying the mass transfer from mountain ranges to deposition in sedimentary basins: Source to sink studies in the Danube Basin–Black Sea system. Glob. Planet. Chang. 103, 1–18. https://doi.org/10.1016/j.gloplacha.2013.01.003

Mayr, C., Stojakowits, P., Lempe, B., Blaauw, M., Diersche, V., Grohganz, M., Correa, M.L., Ohlendorf, C., Reimer, P., Zolitschka, B., 2019. High-resolution geochemical record of environmental changes during MIS 3 from the northern Alps (Nesseltalgraben, Germany). Quat. Sci. Rev. 218, 122–136. https://doi.org/10.1016/j.quascirev.2019.06.013

Ménot, G., Bard, E., Rostek, F., Weijers, J.W., Hopmans, E.C., Schouten, S., Damsté, J.S.S., 2006. Early reactivation of European rivers during the last deglaciation. Science 313, 1623–1625. https://doi.org/10.1126/science.1130511

Milliman, J.D., Farnsworth, K.L., 2013. River discharge to the coastal ocean: a global synthesis. Cambridge University Press.

Milliman, J.D., Syvitski, J.P., 1992. Geomorphic/tectonic control of sediment discharge to the ocean: the importance of small mountainous rivers. J. Geol. 100, 525–544. https://doi.org/10.1086/629606

Misch, D., Wegerer, E., Gross, D., Sachsenhofer, R.F., Rachetti, A., Gratzer, R., 2018. Mineralogy and facies variations of Devonian and Carboniferous shales in the Ukrainian Dniepr-Donets Basin. Aust. J. Earth. Sci. 111, 15–25. https://doi.org/10.17738/ajes.2018.0002

Mol, J., Vandenberghe, J., Kasse, C., 2000. River response to variations of periglacial climate in mid-latitude Europe. Geomorphology 33, 131–148. https://doi.org/10.1016/S0169-555X(99)00126-9

Monegato, G., Ravazzi, C., Donegana, M., Pini, R., Calderoni, G., Wick, L., 2007. Evidence of a two-fold glacial advance during the last glacial maximum in the Tagliamento end moraine system (eastern Alps). Quat. Res. 68, 284–302. https://doi.org/10.1016/j.yqres.2007.07.002

Monegato, G., Scardia, G., Hajdas, I., Rizzini, F., Piccin, A., 2017. The Alpine LGM in the boreal ice-sheets game. Sci. Rep. 7, 2078. https://doi.org/10.1038/s41598-017-02148-7

Mulder, T., Alexander, J., 2001. The physical character of subaqueous sedimentary density flows and their deposits. Sedimentology 48, 269–299. https://doi.org/10.1046/j.1365-3091.2001.00360.x

Mulder, T., Syvitski, J.P., 1995. Turbidity currents generated at river mouths during exceptional discharges to the world oceans. J. Geol. 103, 285–299. https://doi.org/10.1086/629747

Mulder, T., Syvitski, J.P., Migeon, S., Faugeres, J.-C., Savoye, B., 2003. Marine hyperpycnal flows: initiation, behavior and related deposits. A review. Mar. Pet. Geol. 20, 861–882. https://doi.org/10.1016/j.marpetgeo.2003.01.003

Mulder, T., Syvitski, J.P., Skene, K.I., 1998. Modeling of erosion and deposition by turbidity currents generated at river mouths. J. Sedim. Res. 68, 124–137. https://doi.org/10.2110/jsr.68.124

Müller, G., Quakernaat, J., 1969. Diffractometric clay mineral analysis of recent sediments of Lake Constance (Central Europe). Contributions to Mineralogy and Petrology 22, 268–275.

Muttoni, G., Carcano, C., Garzanti, E., Ghielmi, M., Piccin, A., Pini, R., Rogledi, S., Sciunnach, D., 2003. Onset of major Pleistocene glaciations in the Alps. Geology 31, 989–992. https://doi.org/10.1130/G19445.1

NGRIP-members, 2004. High resolution record of Northern Hemisphere climate extending into the last interglacial period. Nature 431, 147–151. https://doi.org/10.1038/nature02805

Nievergelt, P., Liniger, M., Froitzheim, N., Mählmann, R.F., 1996. Early to mid-Tertiary crustal extension in the Central Alps: The Turba mylonite zone (eastern Switzerland). Tectonics 15, 329–340. https://doi.org/10.1029/93TC02312

Nikishin, A.M., Korotaev, M.V., Ershov, A.V., Brunet, M.-F., 2003. The Black Sea basin: tectonic history and Neogene–Quaternary rapid subsidence modelling. Sedim.Geol.156, 149–168. https://doi.org/10.1016/S0037-0738(02)00286-5

Normark, W.R., Piper, D.J., 1991. Initiation processes and flow evolution of turbidity currents: implications for the depositional record. SEPM Special Publications, 46, 207-230

Oerlemans, J., Greuell, W., Denby, B., van de Wal, R., 2001. 10 years of mass-balance measurements along a transect near Kangerlussuaq, central West Greenland. Journal of Glaciology 47, 157–158. https://doi.org/10.3189/172756501781832458

Panin, N., Jipa, D., 2002. Danube River sediment input and its interaction with the north-western Black Sea. Estuar. Coast. Shelf Sci. 54, 551–562. https://doi.org/10.1006/ecss.2000.0664

Panin, N., Panin, S., Herz, N., Noakes, J.E., 1983. Radiocarbon dating of Danube delta deposits. Quat. Res.19, 249–255. https://doi.org/10.1016/0033-5894(83)90008-X

Parajka, J., Kohnová, S., Bálint, G., Barbuc, M., Borga, M., Claps, P., Cheval, S., Dumitrescu, A., Gaume, E., Hlavčová, K., 2010. Seasonal characteristics of flood regimes across the Alpine–Carpathian range. J. Hydrol. 394, 78–89. https://doi.org/10.1016/j.jhydrol.2010.05.015

Pastre, J.-F., Limondin-Lozouet, N., Leroyer, C., Ponel, P., Fontugne, M., 2003. River system evolution and environmental changes during the Lateglacial in the Paris Basin (France). Quat. Sci. Rev. 22, 2177–2188. https://doi.org/10.1016/S0277-3791(03)00147-1

Pellegrini, C., Asioli, A., Bohacs, K.M., Drexler, T.M., Feldman, H.R., Sweet, M.L., Maselli, V., Rovere, M., Gamberi, F., Dalla Valle, G., 2018. The late Pleistocene Po River lowstand wedge in the Adriatic Sea: Controls on architecture variability and sediment partitioning. Mar. Pet. Geol. 96, 16–50. https://doi.org/10.1016/j.marpetgeo.2018.03.002

Pellegrini, C., Maselli, V., Gamberi, F., Asioli, A., Bohacs, K.M., Drexler, T.M., Trincardi, F., 2017. How to make a 350-m-thick lowstand systems tract in 17,000 years: The Late Pleistocene Po River (Italy) lowstand wedge. Geology 45, 327–330. https://doi.org/10.1130/G38848.1

Piper, D.J., Normark, W.R., 2009. Processes that initiate turbidity currents and their influence on turbidites: a marine geology perspective. J. Sedim. Res. 79, 347–362. https://doi.org/10.2110/jsr.2009.046

Popescu, I., Lericolais, G., Panin, N., Normand, A., Dinu, C., Le Drezen, E., 2004. The Danube submarine canyon (Black Sea): Morphology and sedimentary processes. Mar. Geol. 206 (1-4), 249-265. https://doi.org/10.1016/j.margeo.2004.03.003

Popescu, I., Lericolais, G., Panin, N., Wong, H.K., Droz, L., 2001. Late Quaternary channel avulsions on the Danube deep-sea fan, Black Sea. Mar. Geol. 179, 25–37. https://doi.org/10.1016/S0025-3227(01)00197-9

Preusser, F., 2004. Towards a chronology of the Late Pleistocene in the northern Alpine Foreland. Boreas 33, 195–210. https://doi.org/10.1111/j.1502-3885.2004.tb01141.x

Preusser, F., Graf, H.R., Keller, O., Krayss, E., Schlüchter, C., 2011. Quaternary glaciation history of northern Switzerland. Quat. Sci. J. 60, 282–305. https://doi.org/10.3285/eg.60.2-3.06

Rainer, T., Herlec, U., Rantitsch, G., Sachsenhofer, R.F., Vrabec, M., 2002. Organic matter maturation vs clay mineralogy: A comparison for Carboniferous to Eocene sediments from the Alpine-Dinaride junction (Slovenia, Austria). Geologija 45, 513–518.

Rantitsch, G., 1997. Thermal history of the Carnic Alps (Southern Alps, Austria) and its palaeogeographic implications. Tectonophysics 272, 213–232. https://doi.org/10.1016/S0040-1951(96)00259-4

Rasmussen, S. O., Bigler, M., Blockley, S. P., Blunier, T., Buchardt, S. L., Clausen, H., Cvijanovic, I., Dahl-Jensen, D., Johnsen, S. J., Fisher, H., Gkinis, V., Guillevic, M., Hoek, W. Z., Lowe, J. J., Pedro, J. B., Poop, T., Walker, I. K., Wheatley, J. J., Winstrup, M. 2014. A stratigraphic framework for abrupt climatic changes during the Last Glacial period based on three synchronized Greenland ice-core records: refining and extending the INTIMATE event stratigraphy. Quat. Sci. Rev., 106, 14-28. https://doi.org/10.1016/j.quascirev.2014.09.007

Ravazzi, C., Pini, R., Badino, F., De Amicis, M., Londeix, L., Reimer, P.J., 2014. The latest LGM culmination of the Garda Glacier (Italian Alps) and the onset of glacial termination. Age of glacial collapse and vegetation chronosequence. Quat. Sci. Rev. 105, 26–47. https://doi.org/10.1016/j.quascirev.2014.09.014

Reber, R., Akcar, N., Ivy-Ochs, S., Tikhomirov, D., Burkhalter, R., Zahno, C., Lüthold, A., Kubik, P., Vockenhuber, C., Schlüchter, C., 2014. Deglaciation of the Reuss Glacier in the Alps at the end of the Last Glacial Maximum. Swiss Journal of Geosciences 107, 293–307. https://doi.org/110.1007/s00015-014-0169-5

Reimer, P.J., Bard, E., Bayliss, A., Beck, J.W., Blackwell, P.G., Ramsey, C.B., Buck, C.E., Cheng, H., Edwards, R.L., Friedrich, M., 2013. IntCal13 and Marine13 radiocarbon age calibration curves 0–50,000 years cal BP. Radiocarbon 55, 1869–1887. https://doi.org/10.2458/azu_js_rc.55.16947

Reitner, J.M., 2012. Challenges in deciphering the Last Glacial Cycle in Eastern Alps: Examples from the Drau glacier system. Quat. Int. 279, 398. https://doi.org/10.1016/j.quaint.2012.08.1255

Reitner, J.M., 2007. Glacial dynamics at the beginning of Termination I in the Eastern Alps and their stratigraphic implications. Quat. Int. 164, 64–84. https://doi.org/10.1016/j.quaint.2006.12.016

Reuther, A.U., Urdea, P., Geiger, C., Ivy-Ochs, S., Niller, H.-P., Kubik, P.W., Heine, K., 2007. Late Pleistocene glacial chronology of the Pietrele Valley, Retezat Mountains, Southern Carpathians constrained by ^{10}Be exposure ages and pedological investigations. Quat. Int. 164, 151–169. https://doi.org/10.1016/j.quaint.2006.10.011

Revel, M., Ducassou, E., Grousset, F.E., Bernasconi, S.M., Migeon, S., Révillon, S., Mascle, J., Murat, A., Zaragosi, S., Bosch, D., 2010. 100,000 years of African monsoon variability recorded in sediments of the Nile margin. Quat. Sci. Rev. 29, 1342–1362. https://doi.org/10.1016/j.quascirev.2010.02.006

Riboulot, V., Cattaneo, A., Scalabrin, C., Gaillot, A., Jouet, G., Ballas, G., Marsset, T., Garziglia, S., Ker, S., 2017. Control of the geomorphology and gas hydrate extent on widespread gas emissions offshore Romania. Bulletin De La Societe Geologique De France 188 (4), 26. https://doi.org/10.1051/bsgf/2017182

Ross, D.A., Degens, E.T., MacIlvaine, J., 1970. Black Sea: recent sedimentary history. Science 170, 163–165. https://doi.org/10.1126/science.170.3954.163

Ross, D.A., Degens, E.T., 1974. Recent sediments of Black Sea. In: Degens, E.T., Ross, D.A. (Eds.), The Black Sea: Geology, Chemistry, and Biology. American Association of Petroleum Geologists, Tulsa, 183–199.

Rossato, S., Mozzi, P., 2016. Inferring LGM sedimentary and climatic changes in the southern Eastern Alps foreland through the analysis of a ^{14}C ages database (Brenta megafan, Italy). Quat. Sci. Rev. 148, 115–127. https://doi.org/10.1016/j.quascirev.2016.07.013

Ryan, W.B., Major, C.O., Lericolais, G., Goldstein, S.L., 2003. Catastrophic flooding of the Black Sea. Annual Rev. Earth. Planet. Sci.31, 525–554. https://doi.org/10.1146/annurev.earth.31.100901.141249

Ryan, W.B., Pitman III, W.C., Major, C.O., Shimkus, K., Moskalenko, V., Jones, G.A., Dimitrov, P., Gorür, N., Sakinç, M., Yüce, H., 1997. An abrupt drowning of the Black Sea shelf. Mar. Geol. 138, 119–126. https://doi.org/10.1016/S0025-3227(97)00007-8

Sanchez Goñi, M.F., Harrison, S.P., 2010. Millennial-scale climate variability and vegetation changes during the Last Glacial: Concepts and terminology. Quat. Sci. Rev. 29, 2823–2827. https://doi.org/10.1016/j.quascirev.2009.11.014

Schenk, F., Väliranta, M., Muschitiello, F., Tarasov, L., Heikkilä, M., Björck, S., Brandefelt, J., Johansson, A.V., Näslund, J.-O., Wohlfarth, B., 2018. Warm summers during the Younger Dryas cold reversal. Nature Com. 9. https://doi.org/10.1038/s41467-018-04071-5

Sanchi, L., Ménot, G., Bard, E., 2014. Insights into continental temperatures in the northwestern Black Sea area during the Last Glacial period using branched tetraether lipids. Quat. Sci. Rev., 84, 98-108. https://doi.org/10.1016/j.quascirev.2013.11.013

Schmieder, K., Schünemann, B., Schröder, H.G., 2004. Spatial patterns of surface sediment variables in the littoral zone of Lake Constance (Germany). Archiv für Hydrobiologie 161, 455–468. https://doi.org/10.1127/0003-9136/2004/0161-0455

Schramm, J.-M., 1991. The Permian–Triassic of the Gartnerkofel-1 Core (Carnic Alps, Austria): Illite crystallinity in shaly sediments and its comparison with pre-Variscan sequences. Abh Geol BA 45, 69–77.

Schumilovskikh, L. S., Fleitmann, D., Nowaczyk, N. R., Behling, H., Marret, F., Wegwerth, A., Arz, H. W., 2014. Orbital and millenial-scale environmental changes between 64 and 25 ka BP recorded in Black Sea sediments. Clim. Past, 10, 939-945. https://doi.org/10.5194/cp-10-939-2014

Seguinot, J., Jouvet, G., Huss, M., Funk, M., Ivy-Ochs, S., Preusser, F., 2018. Modelling last glacial cycle ice dynamics in the Alps. The Cryosphere Discussions 1–30. https://doi.org/10.5194/tc-2018-8

Sidorchuk, A.Y., Panin, A.V., Borisova, O.K., 2011. Surface runoff to the Black Sea from the East European Plain during Last Glacial Maximum–Late Glacial time. Spec Pap Geol Soc Am 473, 1–25.

Sidorchuk, A.Y., Panin, A.V., Borisova, O.K., 2008. Climate-induced changes in surface runoff on the North-Eurasian plains during the late glacial and Holocene. Water Resources 35, 386–396. https://doi.org/10.1134/S0097807808040027

Simpson, G., Castelltort, S., 2012. Model shows that rivers transmit high-frequency climate cycles to the sedimentary record. Geology 40, 1131–1134. https://doi.org/10.1130/G33451.1

Sionneau, T., Bout-Roumazeilles, V., Biscaye, P.E., Van Vliet-Lanoe, B., Bory, A., 2008. Clay mineral distributions in and around the Mississippi River watershed and Northern Gulf of Mexico: sources and transport patterns. Quat. Sci. Rev. 27, 1740–1751. https://doi.org/10.1016/j.quascirev.2008.07.001

Skinner, L. C., Fallon, S., Waelbroeck, C., Michel, E., & Barker, S., 2010. Ventilation of the deep Southern Ocean and deglacial CO2 rise. Science, 328 (5982), 1147-1151. https://doi.org/10.1126/science.1183627

Smalley, I.J., Leach, J.A., 1978. The origin and distribution of the loess in the Danube Basin and associated regions of east-central Europe: a review. Sed. Geol. 21, 1–26. https://doi.org/10.1016/0037-0738(78)90031-3

Sommerwerk, N., Hein, T., Schneider-Jajoby, M., Baumgartner, C., Ostojic, M.., Paunovic, M., Bloesch, J., Siber, R., Tockner, K, 2009. The Danube River Basin. In: K. Tockner, C.T. Robinson, U. Uehlinger (Eds.), Rivers of Europe, Elsevier Ltd., London, UK (2009), 59-113

Soulet, G., Delaygue, G., Vallet-Coulomb, C., Böttcher, M.E., Sonzogni, C., Lericolais, G., Bard, E., 2010. Glacial hydrologic conditions in the Black Sea reconstructed using geochemical pore water profiles. Earth. Planet. Sci. Lett. 296, 57–66. https://doi.org/10.1016/j.epsl.2010.04.045

Soulet, G., Giosan, L., Flaux, C., Galy, V., 2019. Using Stable Carbon Isotopes to Quantify Radiocarbon Reservoir Age Offsets in the Coastal Black Sea. Radiocarbon 61, 309–318. https://doi.org/10.1017/RDC.2018.61

Soulet, G., Ménot, G., Garreta, V., Rostek, F., Zaragosi, S., Lericolais, G., Bard, E. 2011a. Black Sea "Lake" reservoir age evolution since the Last Glacial-hydrologic and climatic implications. Earth Planet. Sci.Lett., 308(1-2), 245-258. https://doi.org/10.1016/j.epsl.2011.06.002

Soulet, G., Ménot, G., Lericolais, G., Bard, E., 2011b. A revised calendar age for the last reconnection of the Black Sea to the global ocean. Quat. Sci. Rev. 30, 1019–1026. https://doi.org/10.1016/j.quascirev.2011.03.001

Soulet, G., Ménot, G., Bayon, G., Rostek, F., Ponzevera, E., Toucanne, S., Lericolais, G., Bard, E., 2013. Abrupt drainage cycles of the Fennoscandian Ice Sheet. Proc. Natl. Acad. Sci. USA 110, 6682–6687. https://doi.org/10.1073/pnas.1214676110

Spötl, C., Reimer, P.J., Starnberger, R., Reimer, R.W., 2013. A new radiocarbon chronology of Baumkirchen, stratotype for the onset of the Upper Würmian in the Alps: a new radiocarbon chronology of baumkirchen. J. Quat. Sci. 28, 552–558. https://doi.org/10.1002/jqs.2645

Starkel, L., Michczyńska, D.J., Gębica, P., Kiss, T., Panin, A., Perşoiu, I., 2015. Climatic fluctuations reflected in the evolution of fluvial systems of Central-Eastern Europe (60–8 ka cal BP). Quat. Int. 388, 97–118. https://doi.org/10.1016/j.quaint.2015.04.017

Starnberger, R., Drescher-Schneider, R., Reitner, J.M., Rodnight, H., Reimer, P.J., Spötl, C., 2013. Late Pleistocene climate change and landscape dynamics in the Eastern Alps: the inner-alpine Unterangerberg record (Austria). Quat. Sci. Rev. 68, 17–42. https://doi.org/10.1016/j.quascirev.2013.02.008

Starnberger, R., Rodnight, H., Spötl, C., 2011. Chronology of the last glacial maximum in the Salzach Palaeoglacier area (Eastern Alps). J. Quat. Sci. 26, 502–510. https://doi.org/10.1002/jqs.1477

Starnberger, R., Terhorst, B., Rähle, W., Peticzka, R., Haas, J.N., 2009. Palaeoecology of Quaternary periglacial environments during OIS-2 in the forefields of the Salzach Glacier (Upper Austria). Quat. Int. 198, 51–61. https://doi.org/10.1016/j.quaint.2008.06.011

Stoffers, P., Müller, G., 1978. Mineralogy and lithofacies of Black Sea sediments, Leg 42B deep sea drilling project. Initial Reports of the Deep Sea Drilling Project 42, 373–411.

Stroeven, A.P., Hättestrand, C., Kleman, J., Heyman, J., Fabel, D., Fredin, O., Goodfellow, B.W., Harbor, J.M., Jansen, J.D., Olsen, L., 2016. Deglaciation of fennoscandia. Quat. Sci. Rev. 147, 91–121. https://doi.org/10.1016/j.quascirev.2015.09.016

Swierczynski, T., Lauterbach, S., Dulski, P., Delgado, J., Merz, B., Brauer, A., 2013. Mid-to late Holocene flood frequency changes in the northeastern Alps as recorded in varved sediments of Lake Mondsee (Upper Austria). Quat. Sci. Rev. 80, 78–90. https://doi.org/10.1016/j.quascirev.2013.08.018

Tanaka, T., Togashi, S., Kamioka, H., Amakawa, H., Kagami, H., Hamamoto, T., Yuhara, M., Orihashi, Y., Yoneda, S., Shimizu, H., 2000. JNdi-1: a neodymium isotopic reference in consistency with LaJolla neodymium. Chem. Geol. 168, 279–281. https://doi.org/10.1016/S0009-2541(00)00198-4

Toucanne, S., Soulet, G., Freslon, N., Jacinto, R.S., Dennielou, B., Zaragosi, S., Eynaud, F., Bourillet, J.-F., Bayon, G., 2015. Millennial-scale fluctuations of the European Ice Sheet at the end of the last glacial, and their potential impact on global climate. Quat. Sci. Rev. 123, 113–133. https://doi.org/10.1016/j.quascirev.2015.06.010

Toucanne, S., Zaragosi, S., Bourillet, J.F., Cremer, M., Eynaud, F., Van Vliet-Lanoë, B., Pénaud, A., Fontanier, C., Turon, J.L., Cortijo, E., 2009. Timing of massive 'Fleuve Manche'discharges over the last 350 kyr: insights into the European ice-sheet oscillations and the European drainage network from MIS 10 to 2. Quat. Sci. Rev. 28, 1238–1256. https://doi.org/10.1016/j.quascirev.2009.01.006

Toucanne, S., Zaragosi, S., Bourillet, J.-F., Marieu, V., Cremer, M., Kageyama, M., Van Vliet-Lanoë, B., Eynaud, F., Turon, J.-L., Gibbard, P.L., 2010. The first estimation of Fleuve Manche palaeoriver discharge during the last deglaciation: Evidence for Fennoscandian ice sheet meltwater flow in the English Channel ca 20–18 ka ago. Earth Planet. Sci. Lett. 290, 459–473. https://doi.org/10.1016/j.epsl.2009.12.050

Tudryn, A., Leroy, S.A., Toucanne, S., Gibert-Brunet, E., Tucholka, P., Lavrushin, Y.A., Dufaure, O., Miska, S., Bayon, G., 2016. The Ponto-Caspian basin as a final trap for southeastern Scandinavian Ice-Sheet meltwater. Quat. Sci. Rev. 148, 29–43. https://doi.org/10.1016/j.quascirev.2016.06.019

Újvári, G., Kovács, J., Varga, G., Raucsik, B., Marković, S.B., 2010. Dust flux estimates for the Last Glacial Period in East Central Europe based on terrestrial records of loess deposits: a review. Quat. sci. Rev. 29, 3157–3166. https://doi.org/10.1016/j.quascirev.2010.07.005

Újvári, G., Varga, A., Ramos, F.C., Kovács, J., Németh, T., Stevens, T., 2012. Evaluating the use of clay mineralogy, Sr–Nd isotopes and zircon U–Pb ages in tracking dust provenance: An example from loess of the Carpathian Basin. Chem. Geol. 304, 83–96. https://doi.org/10.1016/j.chemgeo.2012.02.007

Urdea, P., 2004. The Pleistocene glaciation of the Romanian Carpathians, in: Developments in Quaternary Sciences. Elsevier, pp. 301–308.

Van Exem, A., Debret, M., Copard, Y., Verpoorter, C., De Wet, G., Lecoq, N., Sorrel, P., Werner, A., Roof, S., Laignel, B., 2019. New source-to-sink approach in an arctic catchment based on hyperspectral core-logging (Lake Linné, Svalbard). Quat. Sci. Rev. 203, 128–140. https://doi.org/10.1016/j.quascirev.2018.10.038

Van Husen, D., 2004. Quaternary glaciations in Austria, in: Developments in Quaternary Sciences. Elsevier, pp. 1–13.

van Husen, D., 2000. Geological processes during the Quaternary. Mitteilungen der Österreichischen Geologischen Gesellschaft 92, 135–156.

Vandenberghe, J., 2003. Climate forcing of fluvial system development: an evolution of ideas. Quat. Sci. Rev. 22, 2053–2060. https://doi.org/10.1016/S0277-3791(03)00213-0

Vandenberghe, J., 2002. The relation between climate and river processes, landforms and deposits during the Quaternary. Quat. Int. 91, 17–23. https://doi.org/10.1016/S1040-6182(01)00098-2

Vidal, L., Menot, G., Joly, C., Bruneton, H., Rostek, F., Çağatay, M.N., Major, C., Bard, E., 2010. Hydrology in the Sea of Marmara during the last 23 ka: Implications for timing of Black Sea connections and sapropel deposition. Paleoceanography 25. https://doi.org/10.1029/2009PA001735

Vishnevskaya, V.S., Sedaeva, K.M., 2000. Specific features of Early-Middle Carboniferous sedimentation in the southern part of the East European Platform. Lithology and Mineral Resources 35, 455–465.

Wang, Y. J., Cheng, H., Edwards, R. L., An, Z. S., Wu, J. Y., Shen, C. C., Dorale, J. A., 2001. A high-resolution absolute-dated late Pleistocene monsoon record from Hulu Cave, China. Science, 294 (5550), 2345-2348. https://doi.org/10.1126/science.1064618

Wegwerth, A., Kaiser, J., Dellwig, O., Shumilovskikh, L. S., Nowaczyk, N. R., Arz, H. W., 2016. Northern hemisphere climate control on the environmental dynamics in the glacial Black Sea 'Lake'. Quat. Sci.Rev. 135, 41-53. https://doi.org/10.1016/j.quascirev.2016.01.016

Wirsig, C., Zasadni, J., Ivy-Ochs, S., Christl, M., Kober, F., Schlüchter, C., 2016. A deglaciation model of the Oberhasli, Switzerland. J. Quat. Sci. 31, 46–59. https://doi.org/10.1002/jqs.2831

Wirth, S.B., Glur, L., Gilli, A., Anselmetti, F.S., 2013. Holocene flood frequency across the Central Alps–solar forcing and evidence for variations in North Atlantic atmospheric circulation. Quat. Sci. Rev. 80, 112–128. https://doi.org/10.1016/j.quascirev.2013.09.002

Wong, H., Panin, N., Dinu, C., Georgescu, P., Rahn, C., 1994. Morphology and post-Chaudian (Late Pleistocene) evolution of the submarine Danube fan complex. Terra Nova 6, 502–511. https://doi.org/10.1111/j.1365-3121.1994.tb00894.x

Wu, H., Guiot, J., Brewer, S., Guo, Z., 2007. Climatic changes in Eurasia and Africa at the last glacial maximum and mid-Holocene: reconstruction from pollen data using inverse vegetation modelling. Climate Dynamics 29, 211–229. https://doi.org/10.1007/s00382-007-0231-3

Yanchilina, A.G., Ryan, W.B.F., McManus, J.F., Dimitrov, P., Dimitrov, D., Slavova, K., Filipova-Marinova, M., 2017. Compilation of geophysical, geochronological, and geochemical evidence indicates a rapid Mediterranean-derived submergence of the Black Sea's shelf and subsequent substantial salinification in the early Holocene. Mar. Geol. 383, 14–34. https://doi.org/10.1016/j.margeo.2016.11.001

Zaragosi, S., Bourillet, J.-F., Eynaud, F., Toucanne, S., Denhard, B., Van Toer, A., Lanfumey, V., 2006. The impact of the last European deglaciation on the deep-sea turbidite systems of the Celtic-Armorican margin (Bay of Biscay). Geo-Mar. Lett. 26, 317–329. https://doi.org/10.1007/s00367-006-0048-9

Zaragosi, S., Eynaud, F., Pujol, C., Auffret, G.A., Turon, J.-L., Garlan, T., 2001. Initiation of the European deglaciation as recorded in the northwestern Bay of Biscay slope environments (Meriadzek Terrace and Trevelyan Escarpment): a multi-proxy approach. Earth. Planet. Sci. Lett. 188, 493–507. https://doi.org/10.1016/S0012-821X(01)00332-6

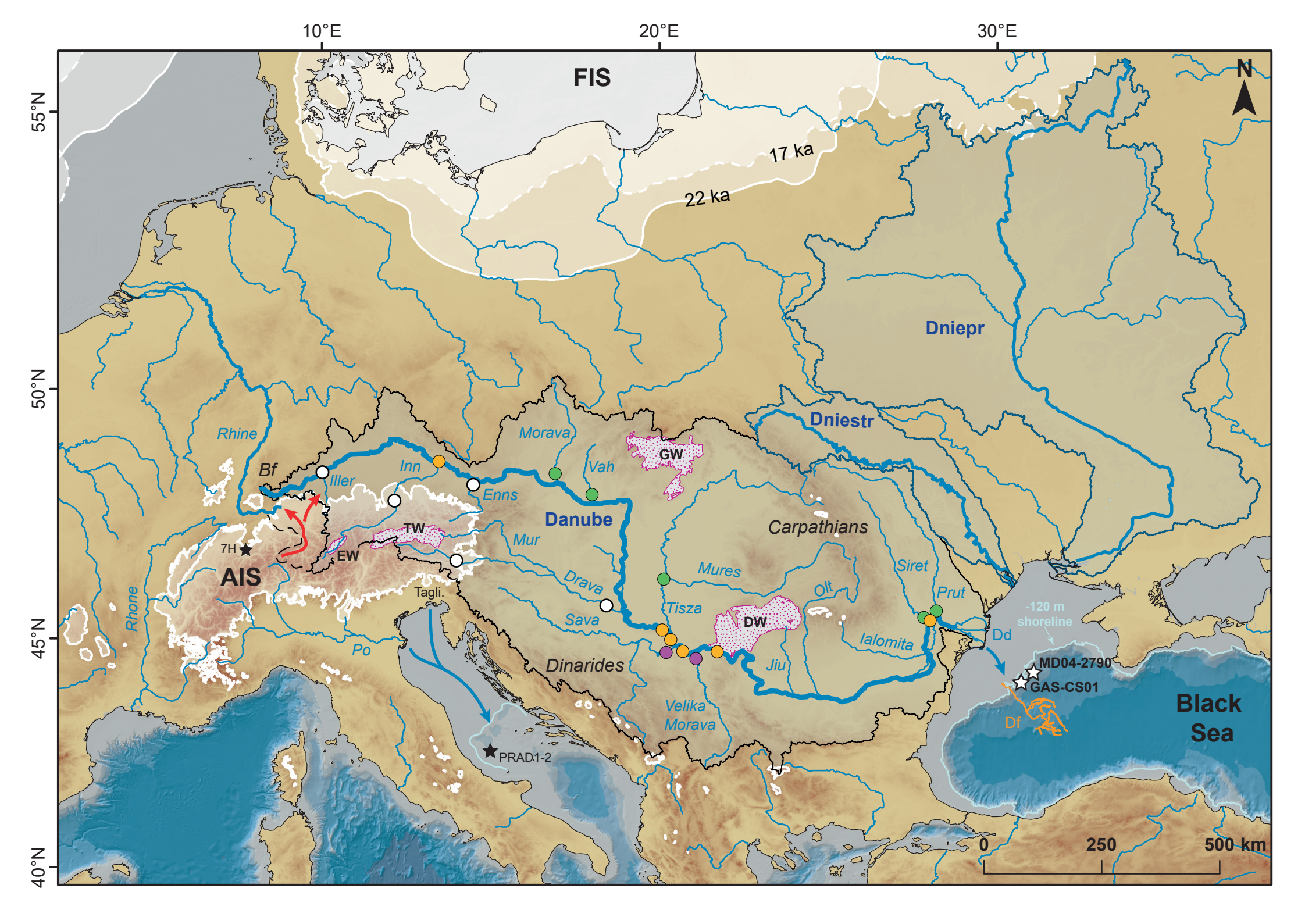
10°E
20°E
30°E
55°N
50°N
45°N
40°N
N
FIS
17 ka
22 ka
Dniepr
Dniestr
Rhine
Bf
Iller
Inn
Enns
Morava
Vah
GW
Danube
Carpathians
Mur
Drava
Sava
Mures
Tisza
DW
Siret
Prut
Olt
Ialomita
Jiu
Dinarides
Velika Morava
Po
Rhone
TW
EW
7H
AIS
Tagli.
PRAD1-2
-120 m shoreline
Dd
Df
MD04-2790
GAS-CS01
Black Sea
0
250
500 km

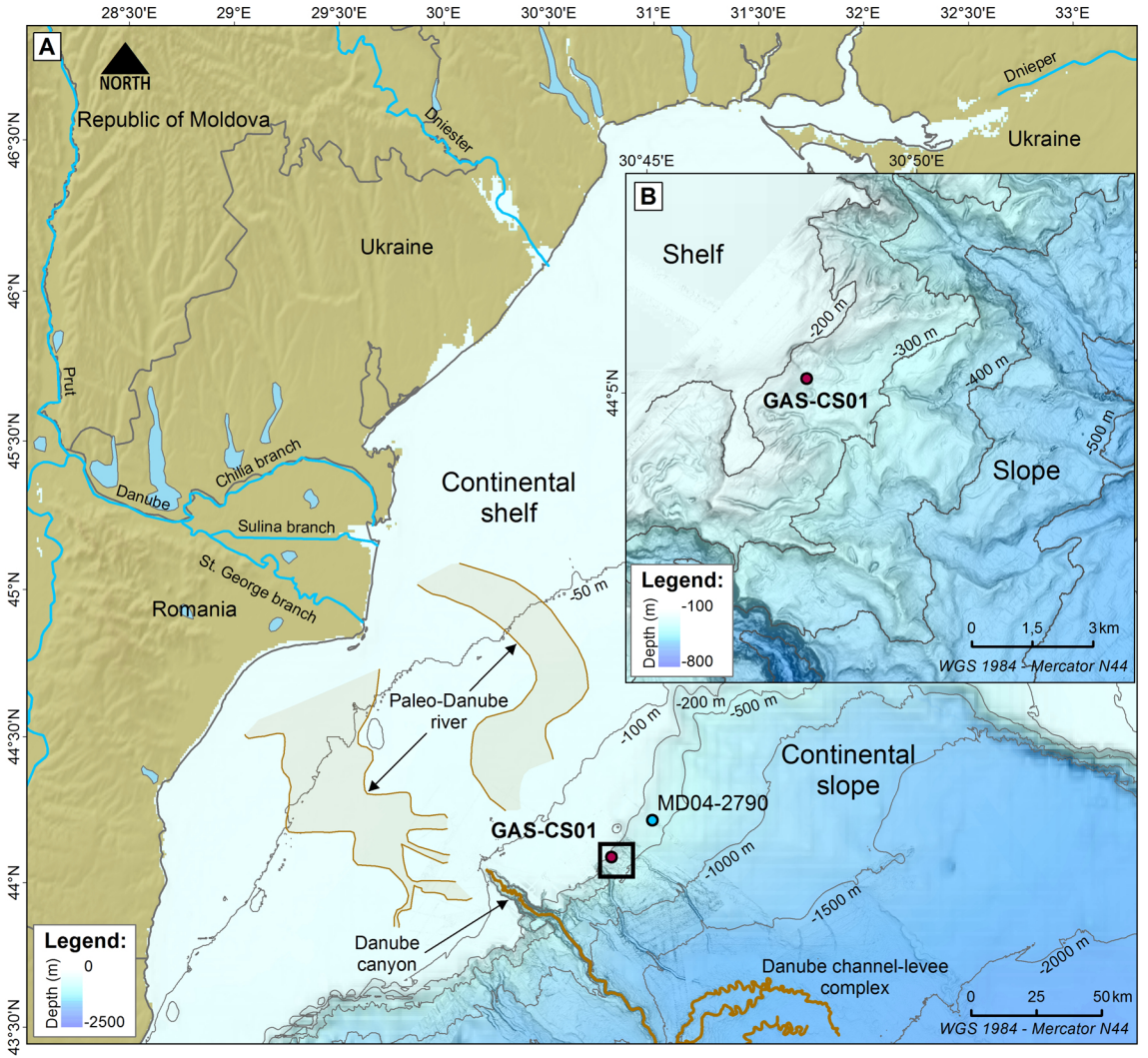
A
NORTH
Republic of Moldova
Ukraine
Dniester
Dnieper
Ukraine
Prut
Chilia branch
Danube
Sulina branch
St. George branch
Romania
Continental shelf
-50 m
Paleo-Danube river
-100 m
-200 m
-500 m
Continental slope
MD04-2790
GAS-CS01
-1000 m
-1500 m
-2000 m
Danube canyon
Danube channel-levee complex
Legend:
Depth (m)
0
-2500
0 25 50 km
WGS 1984 - Mercator N44
B
Shelf
-200 m
-300 m
-400 m
-500 m
GAS-CS01
Slope
Legend:
Depth (m)
-100
-800
0 1,5 3 km
WGS 1984 - Mercator N44
28°30'E
29°E
29°30'E
30°E
30°30'E
31°E
31°30'E
32°E
32°30'E
33°E
30°45'E
30°50'E
46°30'N
46°N
45°30'N
45°N
44°30'N
44°N
44°5'N
43°30'N

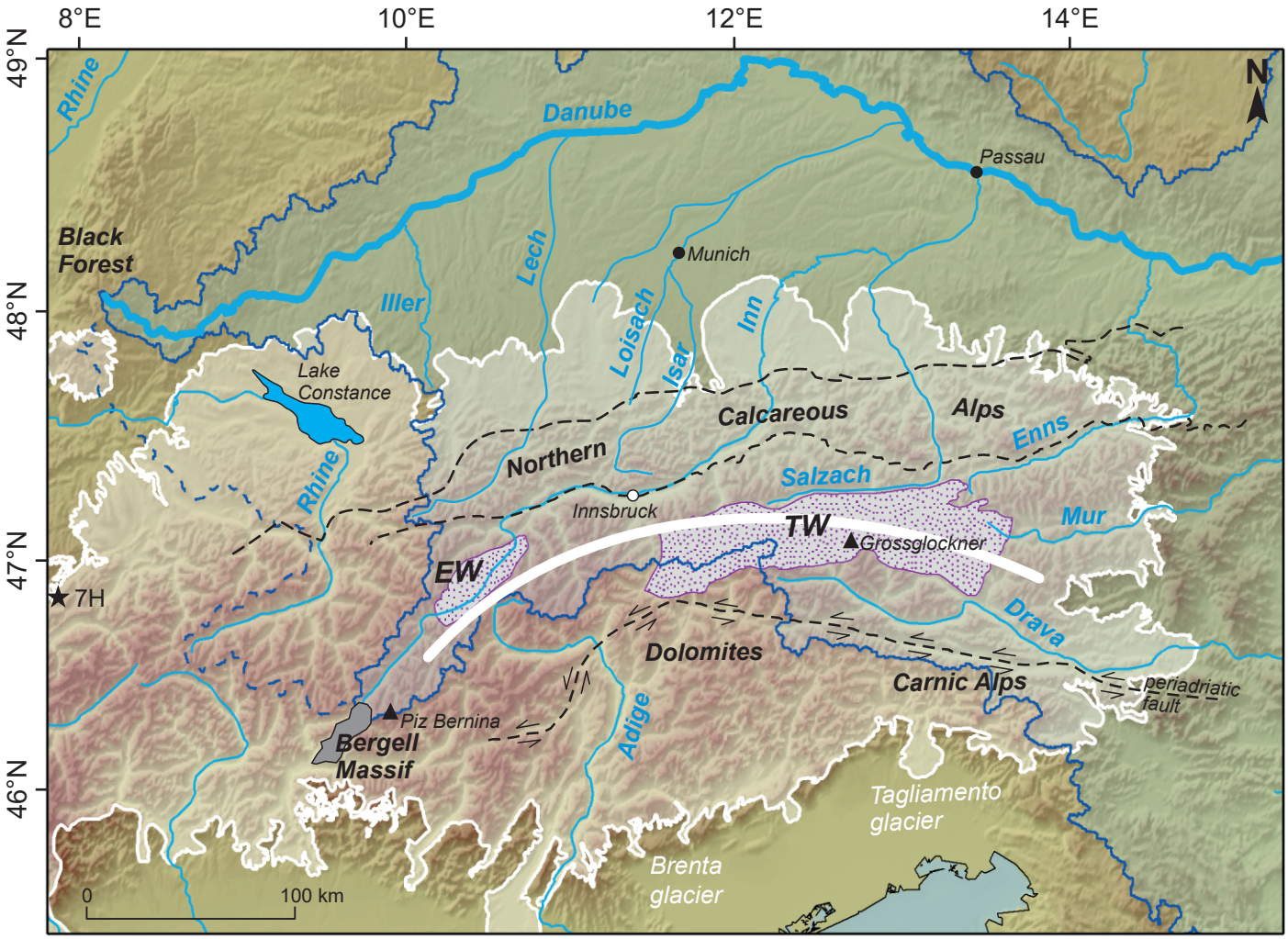
8°E
10°E
12°E
14°E
49°N
48°N
47°N
46°N
N
Rhine
Danube
Passau
Black Forest
Munich
Lech
Iller
Loisach
Isar
Inn
Lake Constance
Calcareous Alps
Enns
Northern
Salzach
Rhine
Innsbruck
TW
Grossglockner
Mur
EW
7H
Drava
Dolomites
Carnic Alps
periadriatic fault
Piz Bernina
Bergell Massif
Adige
Tagliamento glacier
Brenta glacier
0
100 km

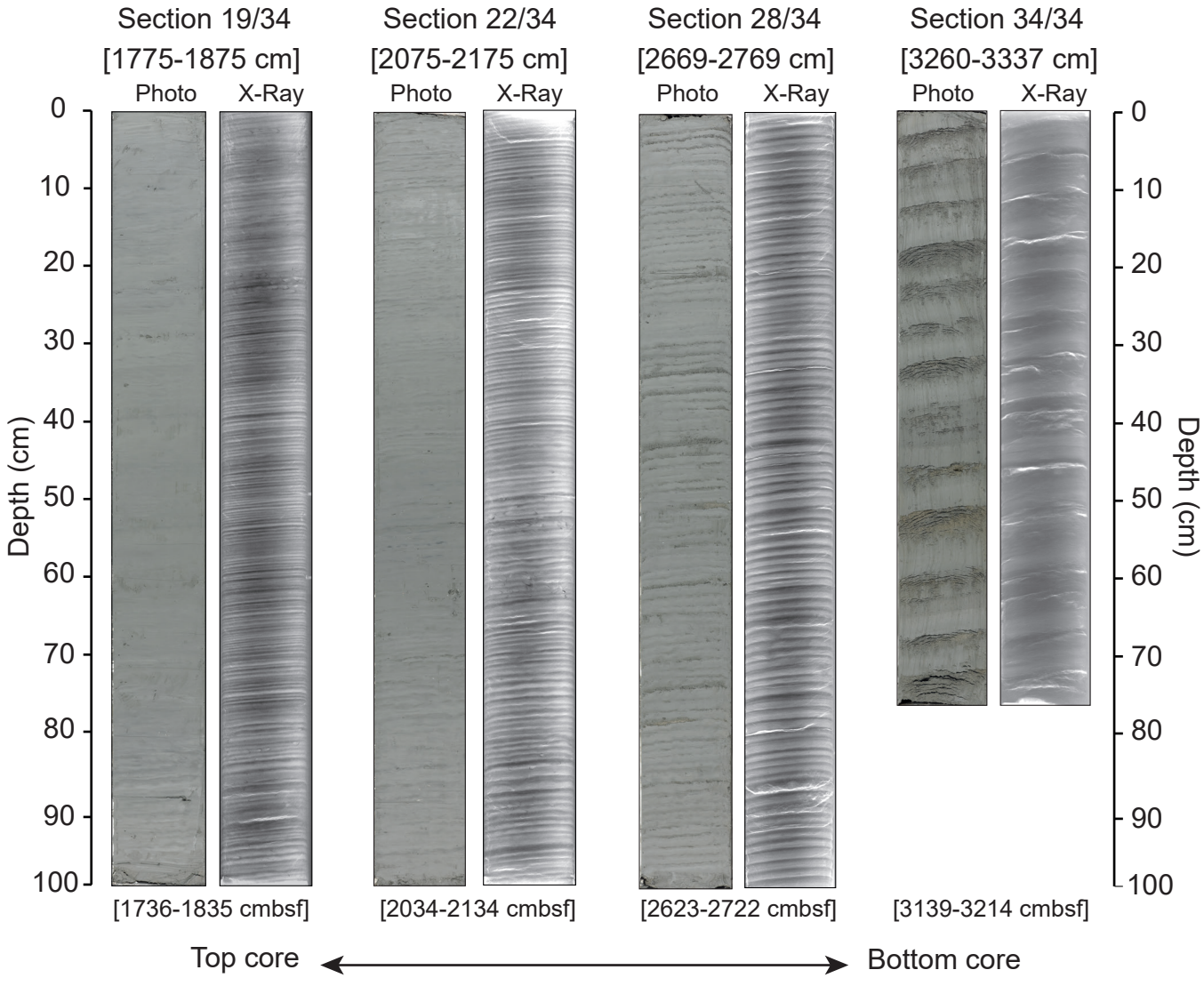
Section 19/34
[1775-1875 cm]
Photo
X-Ray
Section 22/34
[2075-2175 cm]
Photo
X-Ray
Section 28/34
[2669-2769 cm]
Photo
X-Ray
Section 34/34
[3260-3337 cm]
Photo
X-Ray
Depth (cm)
0
10
20
30
40
50
60
70
80
90
100
[1736-1835 cmbsf]
[2034-2134 cmbsf]
[2623-2722 cmbsf]
[3139-3214 cmbsf]
Top core
Bottom core

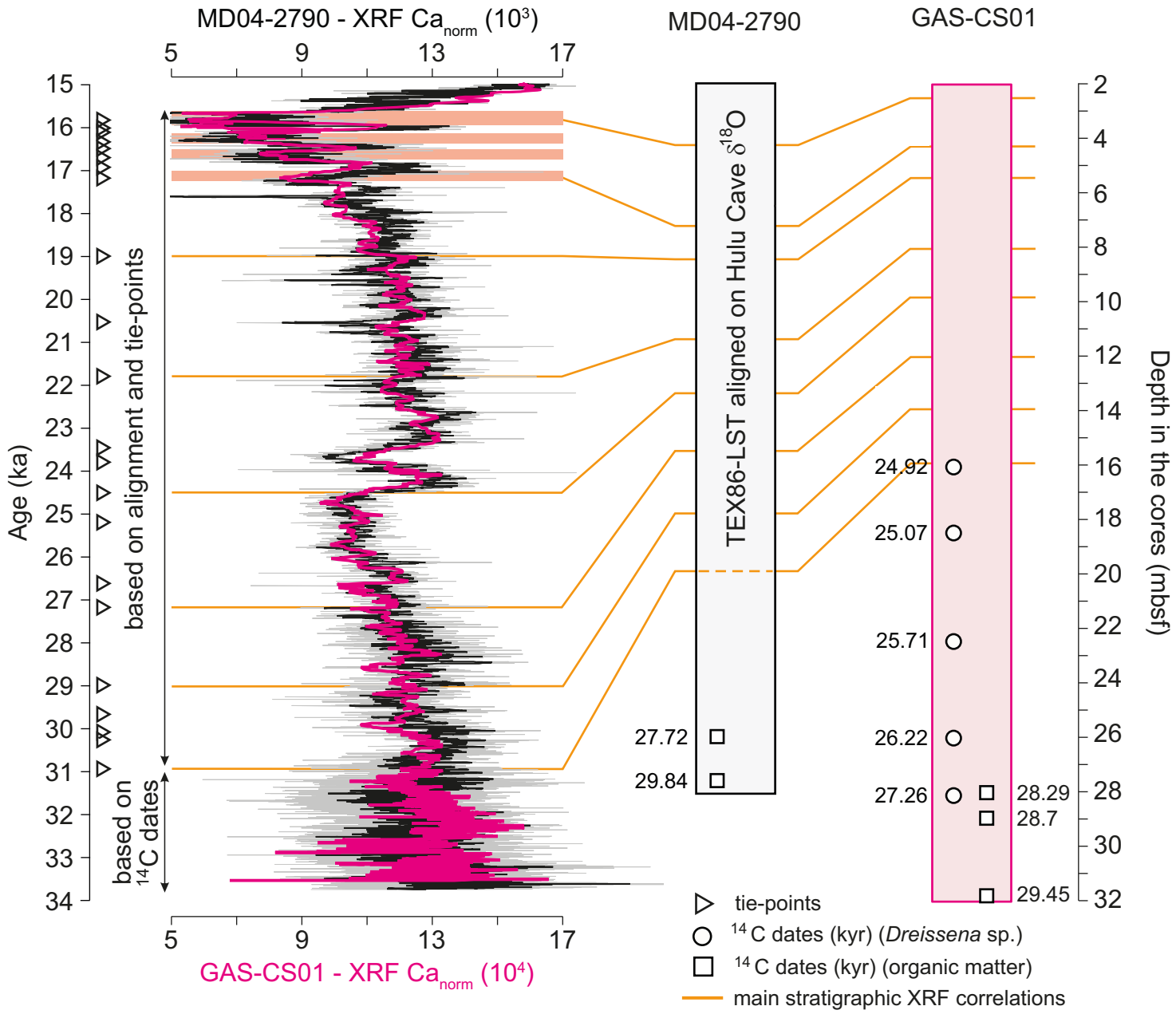
MD04-2790 - XRF Ca$_{norm}$ (10^3)
MD04-2790
GAS-CS01
5
9
13
17
Age (ka)
based on alignment and tie-points
based on ^{14}C dates
TEX86-LST aligned on Hulu Cave δ^{18}O
27.72
29.84
24.92
25.07
25.71
26.22
27.26
28.29
28.7
29.45
Depth in the cores (mbsf)
GAS-CS01 - XRF Ca$_{norm}$ (10^4)
tie-points
^{14}C dates (kyr) (*Dreissena* sp.)
^{14}C dates (kyr) (organic matter)
main stratigraphic XRF correlations

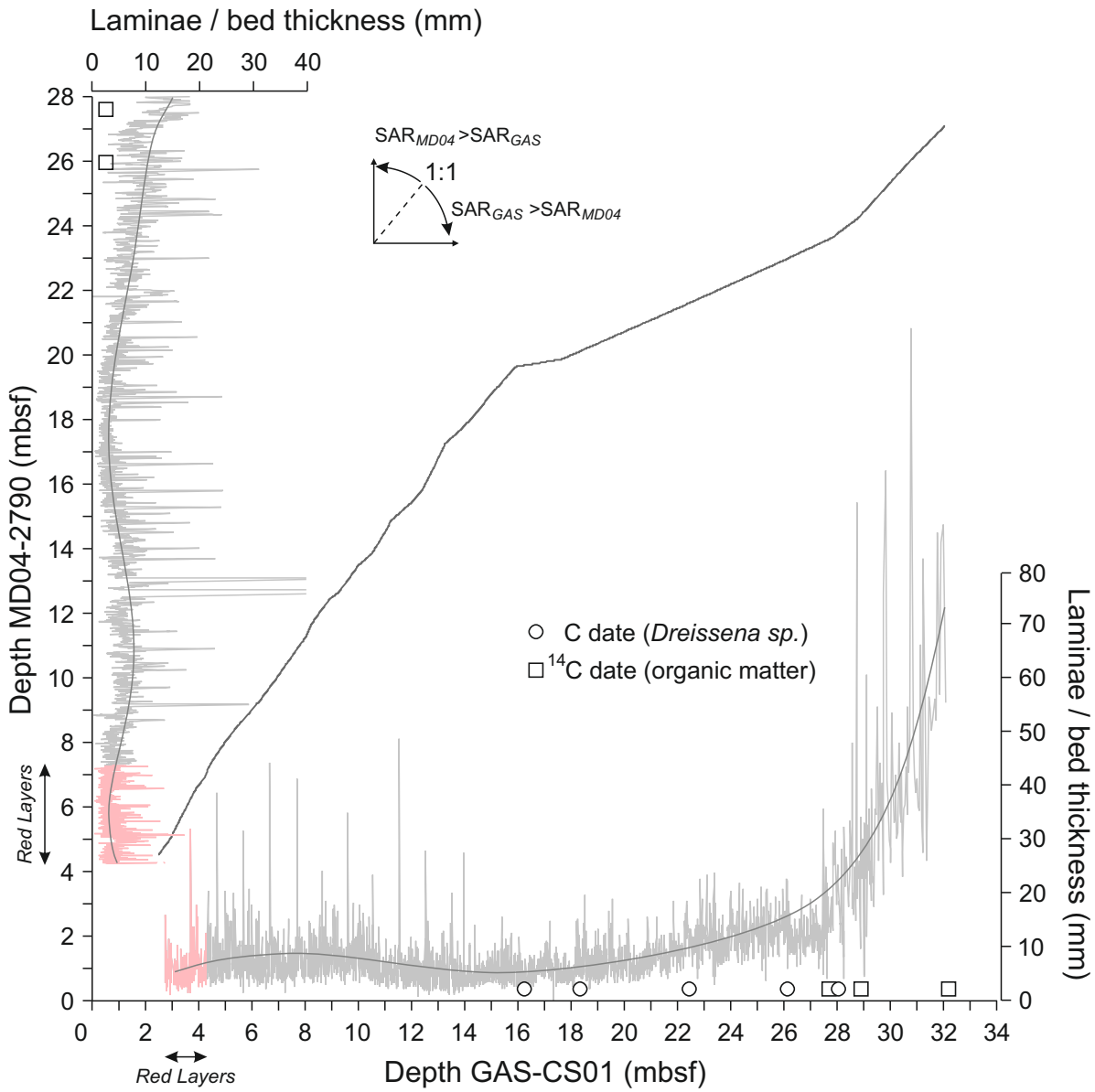
Laminae / bed thickness (mm)
0 10 20 30 40
SAR$_{MD04}$ >SAR$_{GAS}$
1:1
SAR$_{GAS}$ >SAR$_{MD04}$
C date (*Dreissena sp.*)
^{14}C date (organic matter)
Red Layers
Red Layers
Depth MD04-2790 (mbsf)
Depth GAS-CS01 (mbsf)
Laminae / bed thickness (mm)

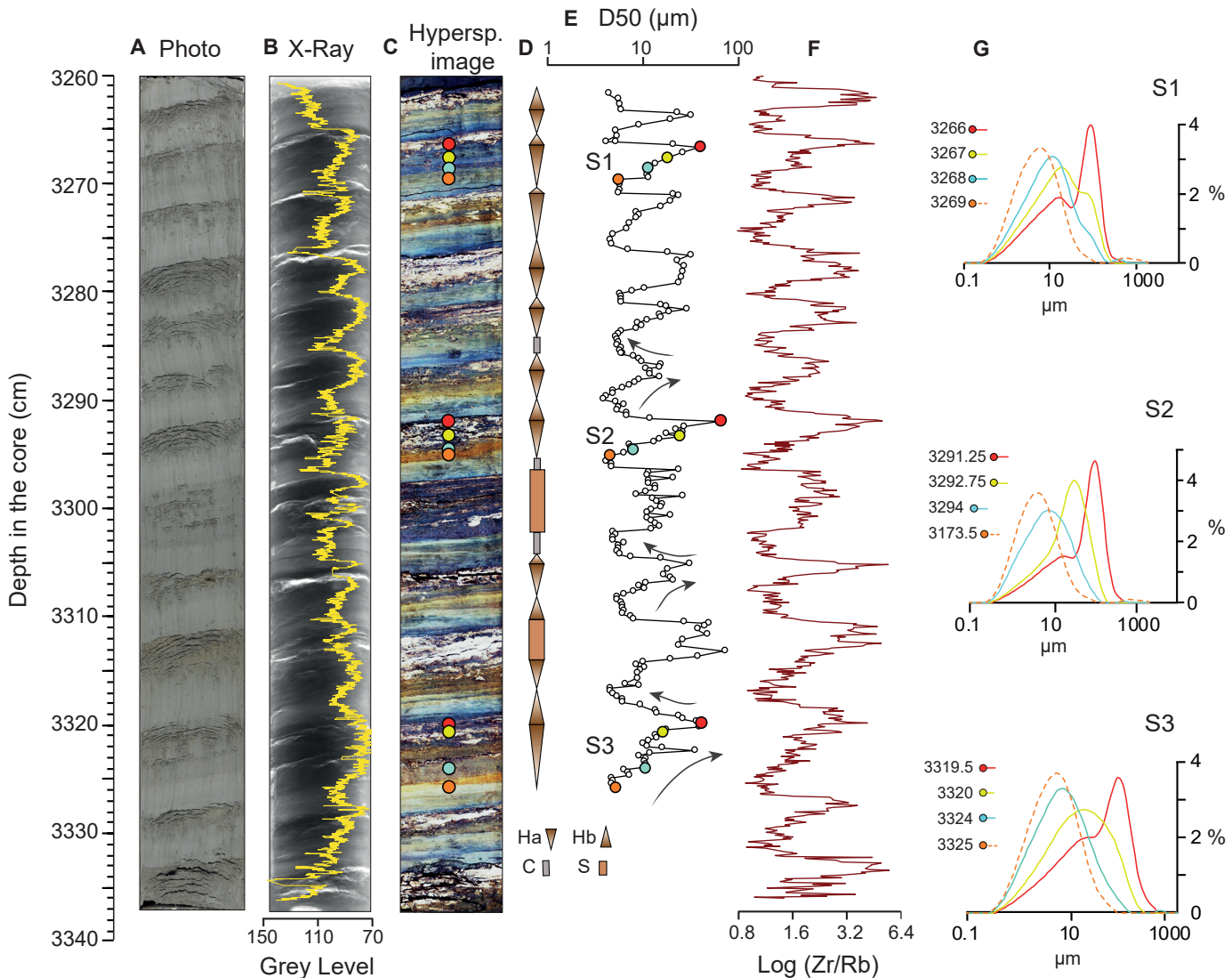
A Photo
B X-Ray
C Hypersp. image
D
E D50 (µm)
1
10
100
F
G
Depth in the core (cm)
3260
3270
3280
3290
3300
3310
3320
3330
3340
150
110
70
Grey Level
S1
S2
S3
Ha
Hb
C
S
0.8
1.6
3.2
6.4
Log (Zr/Rb)
3266
3267
3268
3269
3291.25
3292.75
3294
3173.5
3319.5
3320
3324
3325
0.1
10
1000
µm
%
0
2
4

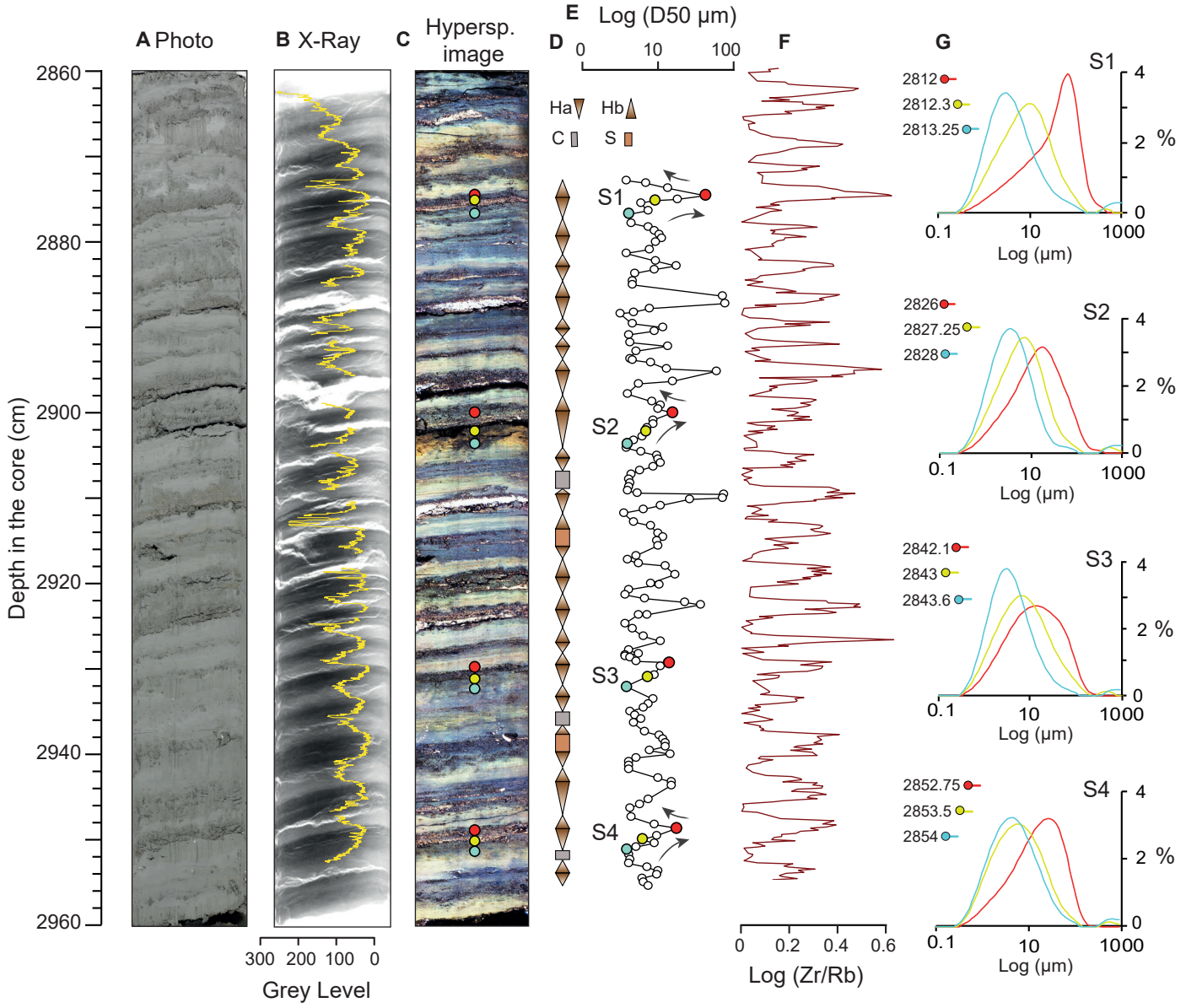
A Photo
B X-Ray
C Hypersp. image
D
E Log (D50 µm)
0
10
100
Ha
Hb
C
S
F
G
Depth in the core (cm)
2860
2880
2900
2920
2940
2960
S1
S2
S3
S4
300 200 100 0
Grey Level
0 0.2 0.4 0.6
Log (Zr/Rb)
2812
2812.3
2813.25
2826
2827.25
2828
2842.1
2843
2843.6
2852.75
2853.5
2854
0.1
10
1000
Log (µm)
4
2
0
%

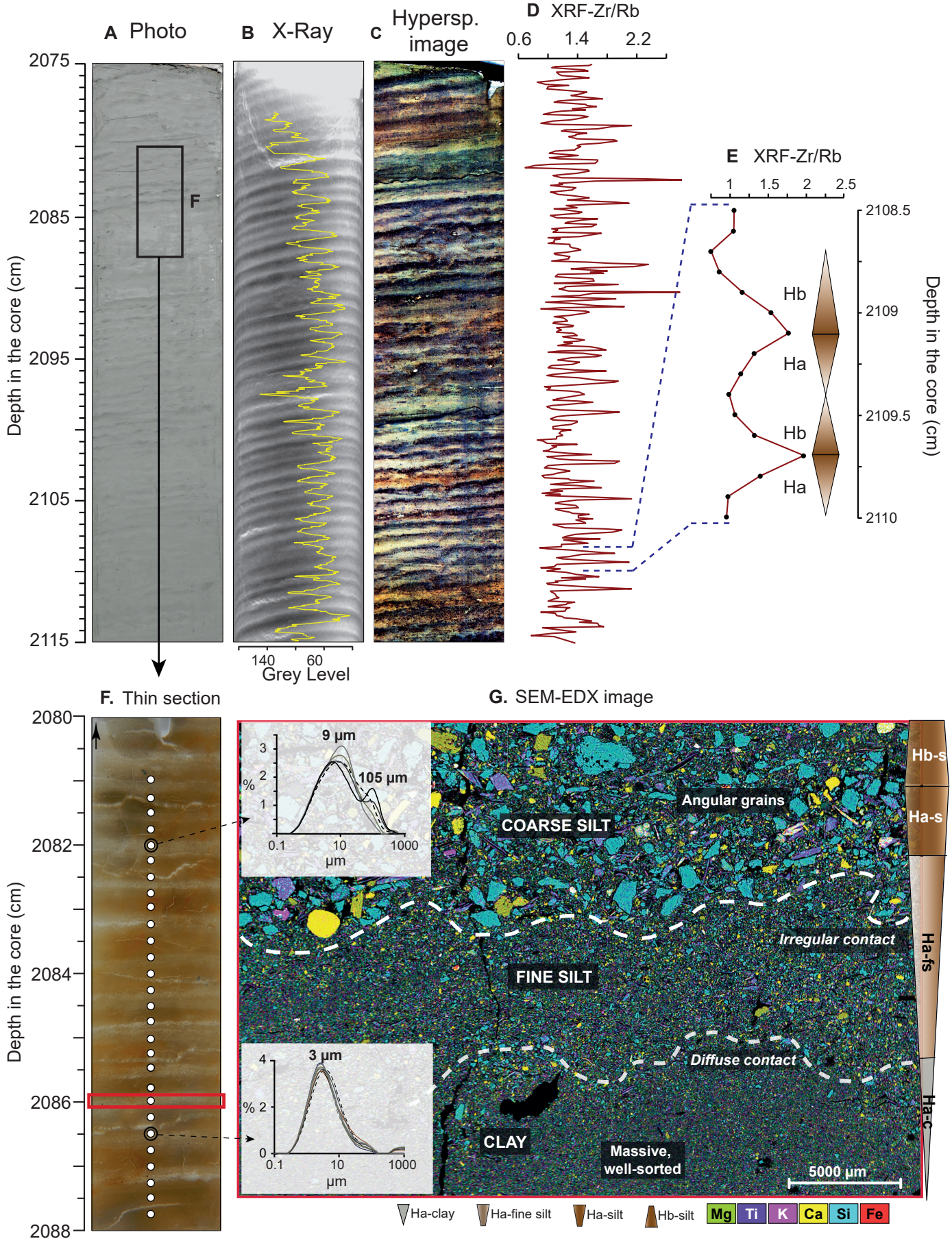
A Photo
B X-Ray
C Hypersp. image
D XRF-Zr/Rb
0.6
1.4
2.2
E XRF-Zr/Rb
1
1.5
2
2.5
F
2075
2085
2095
2105
2115
Depth in the core (cm)
140
60
Grey Level
Hb
Ha
Hb
Ha
2108.5
2109
2109.5
2110
Depth in the core (cm)
F. Thin section
G. SEM-EDX image
2080
2082
2084
2086
2088
Depth in the core (cm)
9 µm
105 µm
%
µm
3 µm
Angular grains
COARSE SILT
FINE SILT
CLAY
Irregular contact
Diffuse contact
Massive, well-sorted
5000 µm
Hb-s
Ha-s
Ha-fs
Ha-c
Ha-clay
Ha-fine silt
Ha-silt
Hb-silt
Mg
Ti
K
Ca
Si
Fe

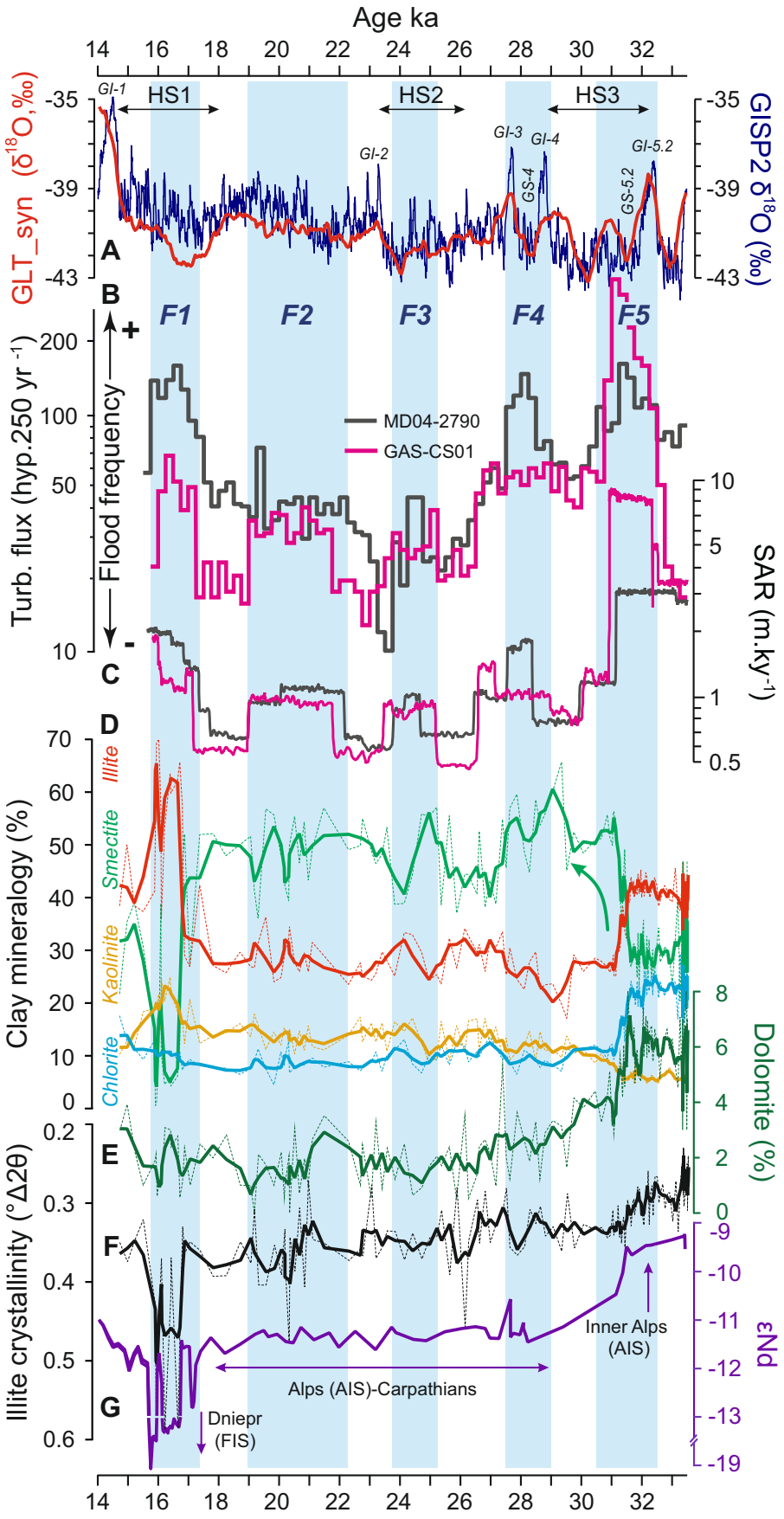
Age ka
14
16
18
20
22
24
26
28
30
32
GLT_syn (δ18O,‰)
GISP2 δ18O (‰)
-35
-39
-43
Gl-1
HS1
HS2
HS3
Gl-2
Gl-3
Gl-4
GS-4
GS-5.2
Gl-5.2
A
B
C
D
E
F
G
F1
F2
F3
F4
F5
Turb. flux (hyp.250 yr -1)
Flood frequency
+
-
200
100
50
10
MD04-2790
GAS-CS01
SAR (m.ky-1)
10
5
1
0.5
Clay mineralogy (%)
Illite
Smectite
Kaolinite
Chlorite
70
60
50
40
30
20
10
0
Dolomite (%)
8
6
4
2
0
Illite crystallinity (°Δ2θ)
0.2
0.3
0.4
0.5
0.6
εNd
-9
-10
-11
-12
-13
-19
Inner Alps
(AIS)
Alps (AIS)-Carpathians
Dniepr
(FIS)

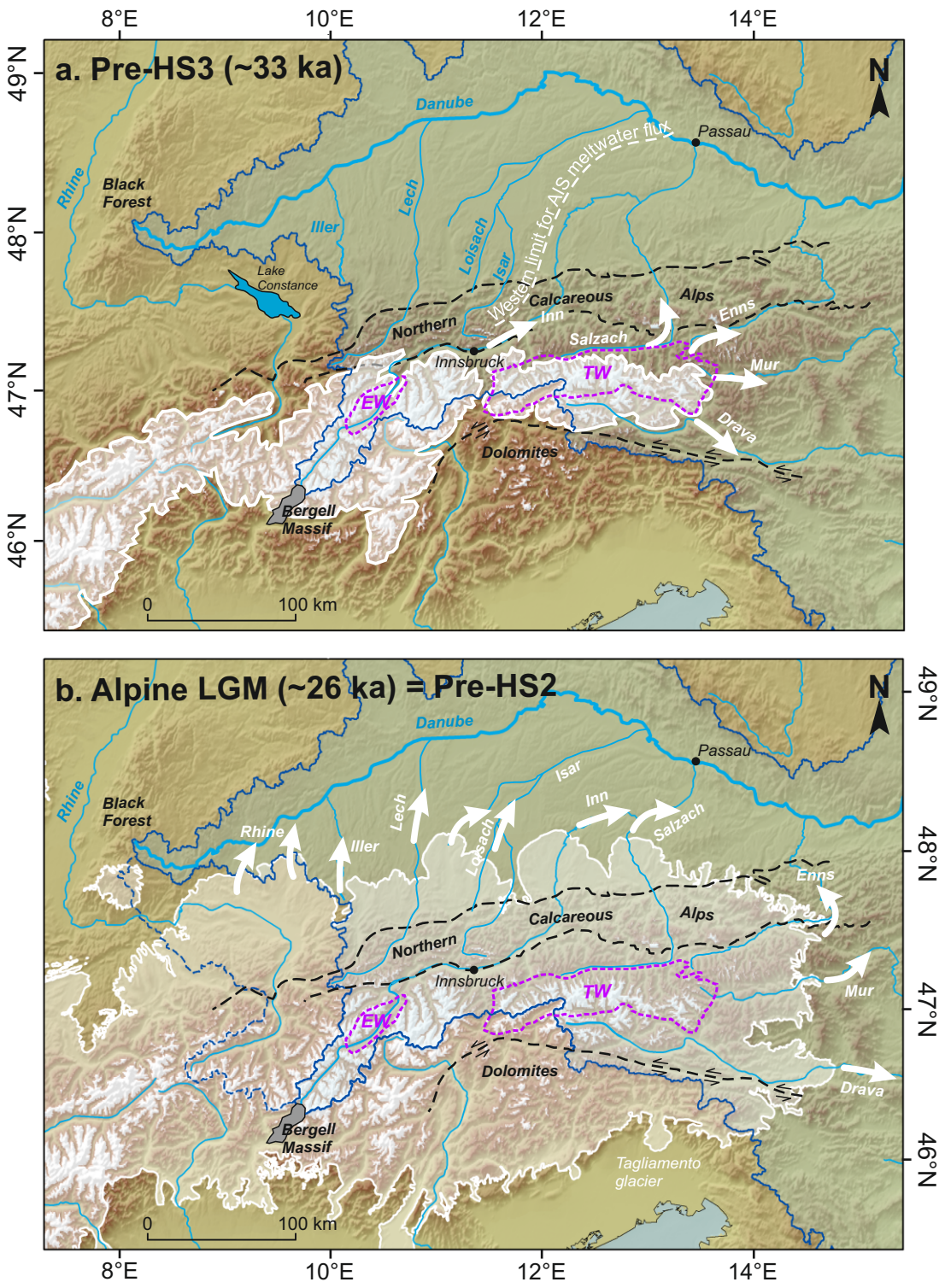
a. Pre-HS3 (~33 ka)
N
8°E
10°E
12°E
14°E
49°N
48°N
47°N
46°N
Danube
Passau
Rhine
Black Forest
Iller
Lech
Loisach
Isar
Western limit for AIS meltwater flux
Lake Constance
Calcareous Alps
Inn
Enns
Northern
Salzach
Innsbruck
TW
EW
Mur
Drava
Dolomites
Bergell Massif
0
100 km
b. Alpine LGM (~26 ka) = Pre-HS2
N
Danube
Passau
Isar
Rhine
Black Forest
Lech
Inn
Salzach
Rhine
Iller
Loisach
Enns
Calcareous Alps
Northern
Innsbruck
TW
EW
Mur
Dolomites
Drava
Bergell Massif
Tagliamento glacier
0
100 km
8°E
10°E
12°E
14°E
49°N
48°N
47°N
46°N

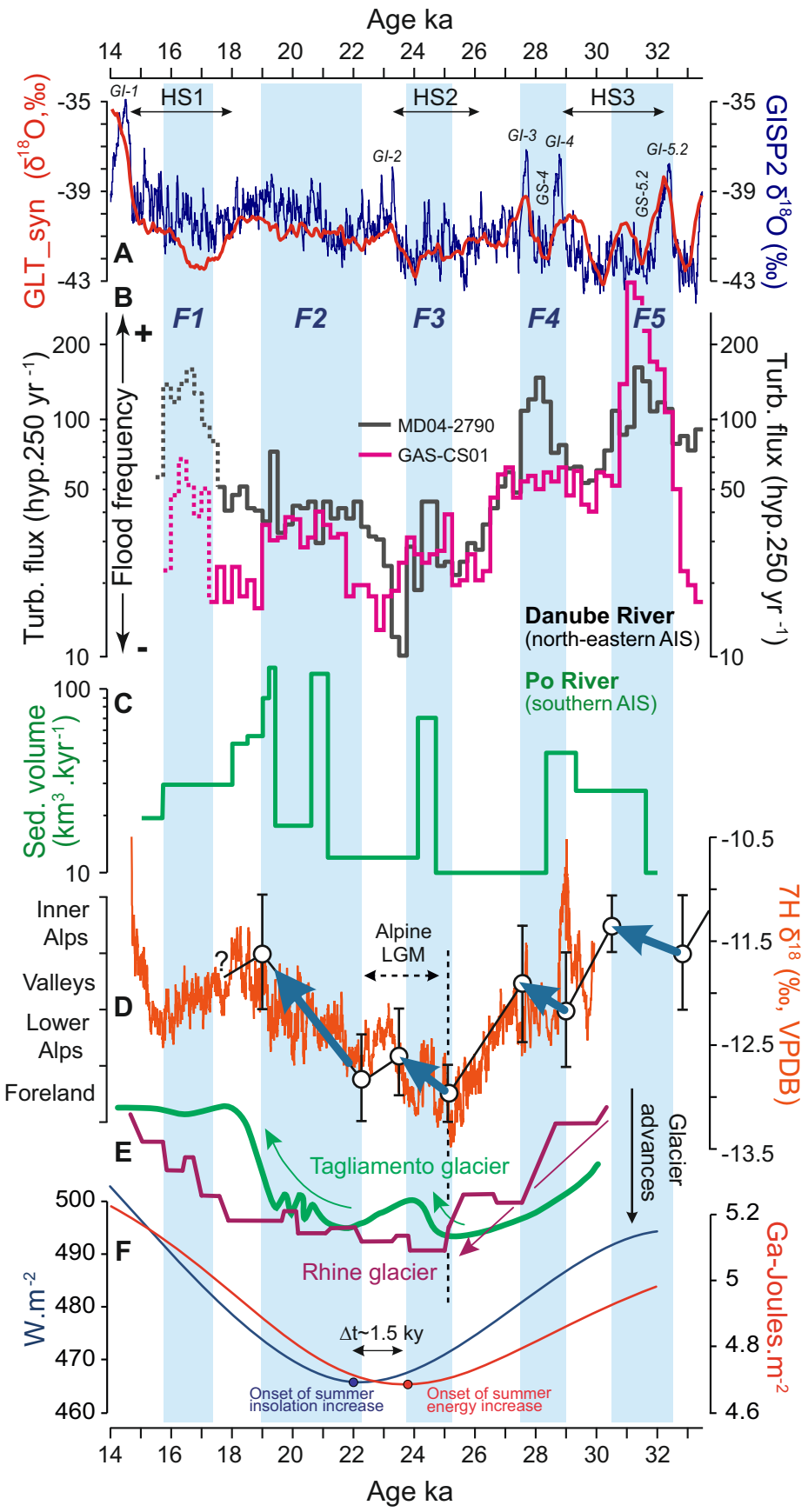
Age ka
14 16 18 20 22 24 26 28 30 32
GLT_syn (δ18O,‰)
GISP2 δ18O (‰)
-35 -39 -43
GI-1
HS1
HS2
HS3
GI-2
GI-3
GI-4
GS-4
GS-5.2
GI-5.2
A
B
F1 F2 F3 F4 F5
Turb. flux (hyp.250 yr-1)
200 100 50 10
+ Flood frequency -
MD04-2790
GAS-CS01
Danube River
(north-eastern AIS)
C
Sed. volume (km3.kyr-1)
100 10
Po River
(southern AIS)
Inner Alps
Valleys
Lower Alps
Foreland
D
?
Alpine LGM
7H δ18 (‰, VPDB)
-10.5 -11.5 -12.5 -13.5
E
Tagliamento glacier
Rhine glacier
Glacier advances
F
W.m-2
500 490 480 470 460
Δt~1.5 ky
Onset of summer insolation increase
Onset of summer energy increase
Ga-Joules.m-2
5.2 5 4.8 4.6
Age ka

Core Label	Lat. N	Long. E	Water depth (m)	Length (m)	Year	Cruise	IGSN
GAS-CS01	44,0865	30,7993	240	33,4	2015	GHASS	http://igsn.org/BFBGX-127384
MD04-2790	44,2219	30,9935	362	30,3	2004	ASSEMBLAGE-1	http://igsn.org/BFBGX-88381

Core ID	Depth (cm)[a]	Depth (cmbsf)[b]	Lab. Number	Sample type	^{14}C age (yr BP)	error (1σ)
GAS-CS01						
GAS-CS01	1651	1614	Beta-440157	*Dreissena* sp.	24,920	120
GAS-CS01	1870	1831	Beta-440158	*Dreissena* sp.	25,070	120
GAS-CS01	2280	2238	Beta-463971	*Dreissena* sp.	25,710	110
GAS-CS01	2650	2604	Beta-463972	*Dreissena* sp.	26,220	110
GAS-CS01	2851	2796	Beta-479030	Organic matter	28,290	120
GAS-CS01	2853	2798	Beta-440160	*Dreissena* sp.	27,260	110
GAS-CS01	2955	2882	Beta-463973	Organic matter	28,700	140
GAS-CS01	3336	3214	Beta-479031	Organic matter	29,450	140
MD04-2790						
MD04-2790	2835	2600	Beta-477223	Organic matter	27,720	130
MD04-2790	3001	2765	Beta-463974	Organic matter	29,840	150

[a] Raw (*i.e.* uncorrected) depth in cores

[b] Corrected depth in cores (*i.e.* after removal of gaps), in cm below sea floor (cmbsf)

River	Drainage area (km²)	Lat. N	Long. E	ICr (°Δ2θ)	Smectite (%)	Illite 2M1 (%)	Kaolinite (%)	Chlorite (%)	Dolomite (%)
Danube Tributaires (*n* =12)									
Alps (n=5)			†	*0.26 ± 0.04*	*9.2 ± 15.4*	*51.2 ± 13.3*	*4.4 ± 1.9*	*28.4 ± 3.8*	*11.2 ± 4.9*
			‡	*0.28 ± 0.04*	*12.2 ± 16.2*	*44.7 ± 12.6*	*5.6 ± 2.2*	*27.8 ± 3.9*	*9.6 ± 5.8*
Iller	26,130	48,36232	10,00110	0,34	40	34	5	21	17
Inn	26,128	47,78181	12,12609	0,28	0	38	3	29	6
Enns	6,185	48,21270	14,48660	0,23	3	65	3	30	17
upper Drava	40,087	46,60046	13,89860	0,2	0	66	3	31	10
lower Drava	40,087	45,69050	18,41658	0,26	3	53	8	31	6
Dinarides (n=2)			†	*0.3 ± 0.04*	*25.5 ± 14.5*	*44.5 ± 9.5*	*17 ± 0*	*14 ± 5*	*1 ± 1*
			‡	*0.28 ± 0.04*	*19.2 ± 15.8*	*48.7 ± 10.4*	*17 ± 0*	*16.2 ± 5.5*	*1.4 ± 1.1*
Sava	95,793	44,72358	20,30960	0,26	11	54	17	19	2
Velika-Morava	37,571	44,60580	21,08620	0,34	40	35	17	9	0
Carpathians (n=5)			†	*0.3 ± 0*	*44.2 ± 25.5*	*34.4 ± 15*	*11.8 ± 7.2*	*9.4 ± 4.5*	*0.8 ± 0.8*
			‡	*0.3 ± 0*	*55.6 ± 28*	*27.6 ± 16.4*	*8.6 ± 7.9*	*7.7 ± 4.8*	*0.3 ± 0.9*
Morava	27,267	48,19118	16,97450	0,3	32	38	21	9	0
Tisza	15,609	46,14687	20,06457	0,3	55	28	8	8	0
Siret	46,289	45,39911	28,01163	0,3	66	22	5	7	1
Prut	28,568	45,47172	28,19500	0,3	68	22	5	5	1
Vah	1,966	47,91403	18,01211	0,3	0	62	20	18	2
Alps + Dinarides + Carpathians (351,593km²)			‡	*0.28 ± 0.01*	*29.6 ± 19.1*	*40.4 ± 9.2*	*10.9 ± 4.9*	*16.6 ± 8.3*	*3.3 ± 4.2*
Danube River (*n* =6)			†	*0.3 ± 0.05*	*29.8 ± 17.5*	*39.6 ± 7.8*	*11 ± 5.5*	*19.5 ± 7.1*	*5.2 ± 1*
Passau	801,093	48,59673	13,38283	0,39	3	41	23	33	0
Upstream Tisza	801,093	45,16503	20,10953	0,28	24	46	8	22	6
Upstream Sava	801,093	44,92347	20,32111	0,33	41	35	9	16	6
Downstream Sava	801,093	44,66575	20,78006	0,27	15	52	11	21	4
Moldava-Noua	801,093	44,69287	21,66701	0,29	42	37	7	14	4
Braila	801,093	45,32294	28,00246	0,25	54	27	8	11	6